Summer 2024

Investigating Accident-Tolerant Cladding in a Molten Salt-Cooled Micro-Reactor using Multi-Physics Analysis and Uncertainty Quantification

Alexander Niles Foutch
Missouri University of Science and Technology

Department:

INVESTIGATING ACCIDENT-TOLERANT CLADDING IN A MOLTEN SALT-COOLED MICRO-REACTOR USING MULTI-PHYSICS ANALYSIS AND UNCERTAINTY QUANTIFICATION

by

ALEXANDER NILES FOUTCH

A THESIS

Presented to the Graduate Faculty of the

MISSOURI UNIVERSITY OF SCIENCE AND TECHNOLOGY

In Partial Fulfillment of the Requirements for the Degree

MASTER OF SCIENCE

in

NUCLEAR ENGINEERING

2024

Approved by:

Ayodeji Alajo, Advisor
Syed Bahauddin Alam
Dinesh Kumar

ABSTRACT

Renewed interest in nuclear safety has resulted in development of accident-tolerant materials, such as cladding. Although developed for light water reactors, their use in more advanced reactors would save time and development costs for other new materials. This paper performed a multiphysics investigation into the power profile, thermodynamics, heat transfer, and tensor mechanics of four candidate materials (Haynes 230, Zircaloy-4, FeCrAl, and SiC-SiC), using the highly benchmarked Kilopower design as an example of a high-temperature, highly-enriched, sodium-cooled microreactor environment.

From neutronic code MCNP, no signifcant difference in power profile was found among the four. Using finite element software framework MOOSE, temperature convergence and pipe rupture analysis using hoop stress were performed. SiC-SiC displayed the most resistance to temperature change, although more noteworthy was Haynes 230 (the default material in Kilopower), the best performing candidate during stress analysis. The high temperatures had the most impact on these results, greatly affecting Zircaloy-4 and FeCrAl's material limits, while SiC-SiC's inelastic, ceramic nature was non-conducive to the stress loads it experienced.

Also investigated was the possibility of variance in the material properties. The impact of Young's Modulus and Poisson's Ratio on maximum hoop stress were measured with uncertainty quantification and sensitivity analysis using polynomial chaos expansion and Sobol' indices, respectively. No significant sensitivities were found, although Zircaloy-4 was close to performing under stress limits, and further investigation into its properties is recommended.

A recommendation is put forth for more research into the high temperature properties of further existing materials for a more robust conclusion on their applicability to advanced reactors, although Haynes 230 is recommended as the current best in the tested areas.

ACKNOWLEDGMENTS

This project would like to thank many people for their support towards its completion. It would not have been possible without them.

My deepest thanks to my advisors Dr. Syed Bahauddin Alam and Dr. Ayodeji Alajo, who gave much-appreciated guidance toward this topic and the methodology of multiphysics M&S and UQ / SA. Additionally, a thank you to my third committee member, Dr. Dinesh Kumar, who provided much-needed assistance on the UQ / SA process and its engineering applications. And a special thanks to Dr. Joshua Schlegel and James Daniell, members of the Missouri S&T nuclear engineering department who provided their generous advice at various steps of this project.

This research made use of Idaho National Laboratory computing resources, which are supported by the Office of Nuclear Energy of the U.S. Department of Energy and the Nuclear Science User Facilities under Contract No. DE-AC07-05ID14517. It also made use of the Foundry, Missouri S&T's high performance computing supercluster.

TABLE OF CONTENTS

Page

LIST OF ILLUSTRATIONS

LIST OF TABLES

NOMENCLATURE

Nomenclature	Meaning
APP	Axial Power Profile
ATC	Accident-tolerant cladding
ATF	Accident-tolerant fuel
BC	Boundary condition
FS	Fracture Strength
HEU	Highly-enriched Uranium
HP#	Heat Pipe 1, 2, or 3
HPC	High Performance Computing
HTC	Heat transfer coefficient
INL	Idaho National Laboratory
KRUSTY	Kilopower Reactor Using Stirling TechnologY
LOCA	Loss of coolant accident
LWR	Light water-cooled reactor
M&S	Modeling and simulation
MCNP	Monte Carlo N-Particle Transport
MLI	Multi-layer insulation
MOOSE	Multiphysics Object Oriented Simulation Environment
MSR	Molten salt reactor
NASA	National Aeronautics and Space Administration
NOC	Normal operational conditions
PCE	Polynomial Chaos Expansion
PDF	Probability Density Function
PR	Poisson's Ratio
RCx	Ring Clamp A through F

SA	Sensitivity analysis
SCF	Stress concentration factor
SiC	Silicon-Carbide
UQ	Uncertainty quantification
YM	Young's Modulus
YS	Yield Strength

1. INTRODUCTION

1.1. BACKGROUND AND MOTIVATION

Since the incident at Fukushima Daiichi nuclear power plant in 2011, there has been a renewed interest in nuclear innovations for accident prevention, much of it directed at the materials used for uranium fuel and fuel rod claddings. These accident-tolerant fuels and claddings (ATFs and ATCs) are mainly under development for application to light water-cooled reactors (LWRs), a classification to which Fukushima and most other commercial nuclear power plants belong [8] [9].

Claddings designated as 'accident-tolerant' exhibit a particular resistance to oxidation. In an LWR accident scenario where higher levels of steam enter the coolant system, this resistance would reduce heat generation from that chemical process and in doing so delay core degradation [10]. This is, however, not the only advantage they may present in terms of 'accident-tolerance.' This paper will explore those other advantages.

Such new materials take long periods of time to be fabricated, tested, and implemented. The landscape of nuclear power production is also changing, with the advent of advanced and small modular reactor designs that are very different from existing LWRs [10].

In the interest of saving future development time on claddings for advanced / small modular reactors, this project seeks to examine the performance of candidate ATCs in such an environment. Compared to LWRs, this will impact the temperatures, pressures, irradiation, and stresses experienced by cladding. This includes experiences at normal operational conditions (NOC) and during a loss of coolant accident (LOCA). This will mainly measure the materials' proximities to failure limits during simulation, comparing the candidates' fractions of performance vs limit between each other and determining which is least likely to reach those limits (or which already exceed them).

Table 1.1. Characteristics of a Typical LWR vs Kilopower

	Typical LWR [9] [14]	Kilopower [2]
Fuel	UO2	U8Mo
Enrichment	4%	õ3%
Operating Power (th)	700 MWe	1-10 kWe
Coolant	Light water (two-phase)	Sodium (two-phase)
Cladding	Zirconium alloy	Haynes 230

As the name suggests, a LOCA occurs when coolant is blocked or diverted and is not able to flow through the reactor core. This leads to higher temperatures and pressures than the cladding is designed for and may even lead to dangerous levels of thermal expansion and / or eventual rupture, releasing irradiated coolant, and potentially a meltdown, if coolant flow cannot be restored. Of the common cladding failure modes, LOCAs were chosen for analysis due to their relation to the aforementioned design-basis of ATCs [11]. They also present a very real opportunity for extreme conditions in which to place the candidate claddings. And it is the very same incident that cascaded into the disaster at Fukushima [12] [13].

1.2. KILOPOWER / KRUSTY

In terms of existing concepts, the Kilopower reactor developed at NASA Glenn is a good base. It is a fission surface power (FSP) micro-reactor, designed to be part of a lunar colony's electric grid [2]. This necessitates many differences from commercial LWRs, detailed in Table 1.1.

More specifically, as seen in Figure 1.1, Kilopower's fuel is monolithic, made of three separately-wrought cylindrical blocks of U8Mo (Uranium with 8% Molybdenum) fuel, coming together at 25 *cm* long axially. A B4C (Boron Carbide) control rod is inserted into a central hole in the fuel. It is the reactor's only moving part. Within outer gaps in the

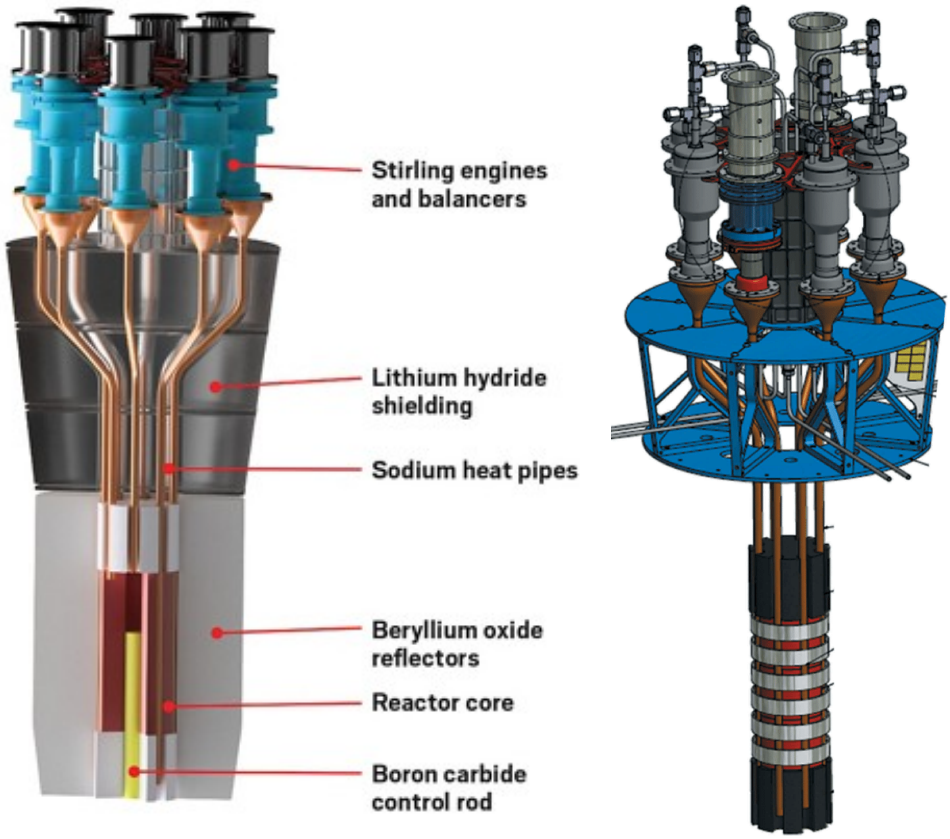

Figure 1.1. Two renders of the in-flight Kilopower system. [1] [2].

fuel are inserted eight heat pipes in angular symmetry. The pipes themselves are made of Haynes 230, with a thin inner layer of nickel as a wick against in-flowing two-phase sodium coolant and a thin outer layer of copper foil to prevent mass diffusion/transfer between the U8Mo and the Haynes 230 at operational temperatures. Seven equally-spaced ring clamps surround the fuel and heat pipes, providing both thermal and structural coupling. All these components are held together via an interference fit - heating the clamps to high temperature, expanding them, and allowing them to cool around the core until they are all firmly pressed together [2].

This compact design was chosen to minimize volume / mass during transport into and throughout space and to provide modularity, allowing it to be combined with other Kilopowers to satisfy a power system's needs. Hence its use of highly-enriched uranium (HEU), which allowed for higher power density from the fuel. Heat pipes also eliminated the need for pumps to drive the flow of coolant [2], further condensing the load.

These design decisions set very different conditions for its structural components to satisfy. For instance, an LWR often has its uranium fuel encased in cladding, a protective outer layer, separated with a small gas gap to allow thermal expansion of the uranium fuel. This design has no such precaution, meaning that the Kilopower fuel will not only experience a greater rate of heat transfer from it to its heat pipes, but the rest of the core must be able to sustain the fuel's thermal expansion directly.

Kilopower is a particularly helpful benchmark for this project, having been recently and extensively tested [2] [15]. Results of the Kilopower Reactor Using Stirling TechnologY (KRUSTY) Nuclear Ground Test conducted on March 21, 2018 are readily available. KRUSTY has slight differences in configuration from the default Kilopower 'flight' set-up. These changes are negligible for this analysis, but the KRUSTY configuration will be prioritized unless specified otherwise.

The test configuration adds several outer layers that aren't in the initial Kilopower design, pictured in Figures 1.2 and 1.3. Multi-layer insulation (MLI), composed of Molybdenum foil, prevents significant heat loss from the core and a stainless steel vacuum can simulates the environment of both outer space and the lunar surface. Both designs include a large, cylindrical BeO (Beryllium Oxide) reflector / shield around the entire core apparatus. Although KRUSTY's is broken into a platen, a shim, and an axial section, they are roughly of equal shape and size. A thin stainless steel sleeve inside the shield ensures alignment and prevents contact with the vacuum can [2].

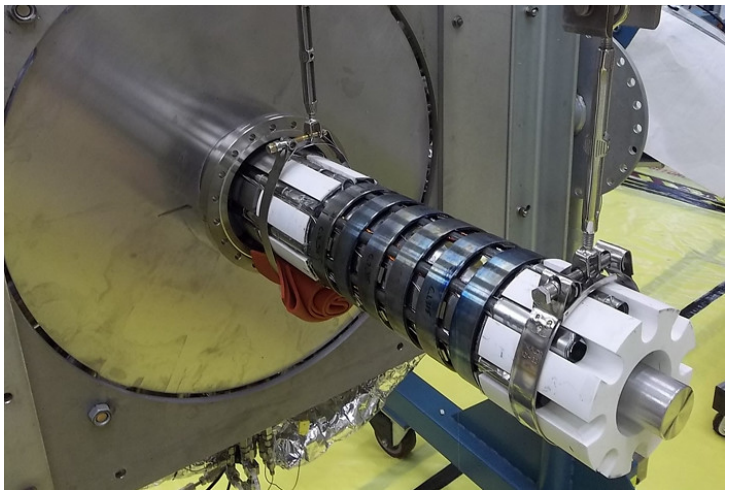

Figure 1.2. Fully-assembled Kilopower Reactor Using Stirling TechnologY (KRUSTY) Nuclear Ground Test core [3].

If it were simply a concept, tested only through M&S, unforeseen factors may force redesigns, such as unknown chemical interactions under high temperatures, pressures, and irradiation. Having verification of this design's viability lends Kilopower an authenticity for what can be expected of some advanced, non-LWR reactors, such as its choice of heat pipes, sodium coolant, a monolithic core, etc. To name an example, this is particularly what could be expected from NASA, the design's patron, which is currently investigating advanced reactors for its own use [16]. If Kilopower (or technology based on it) is to be deployed as part of NASA's already-in-progress Artemis Plan, then the sooner the optimum materials are ready, the better [17]. And any other programs using KRUSTY-like microreactors can look to that design and this analysis for their use.

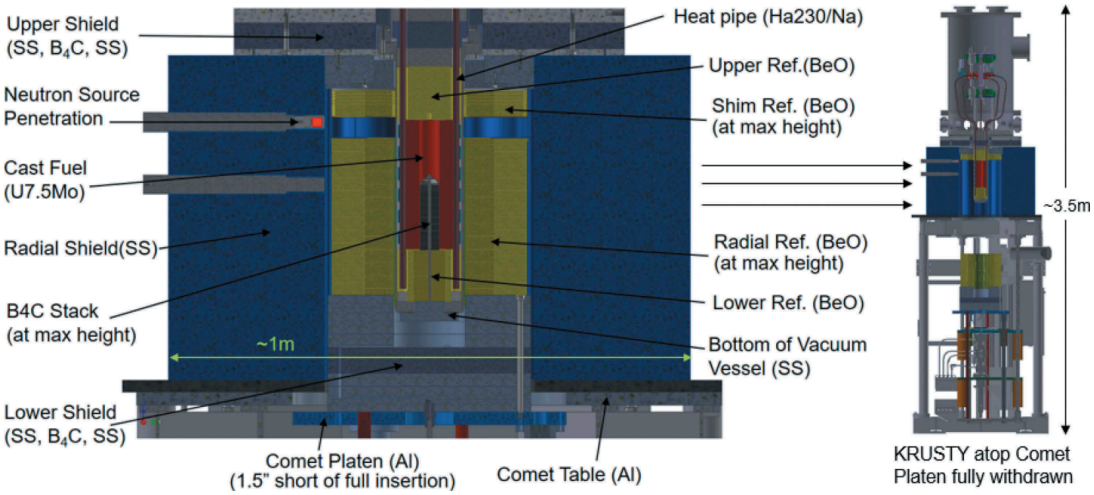

Figure 1.3. KRUSTY configuration [2].

2. METHODOLOGY

2.1. KILOPOWER APPLICATIONS

On the application of ATCs to Kilopower, this reactor is not designated as having a 'cladding' [2]. However, the general purposes of nuclear fuel cladding are to:

- Transfer heat and prevent corrosion between coolant and fuel
- Contain swelling of fuel pellets

Looking at Kilopower's design, these roles are achieved by its eight heat pipes and a series of ring clamps that surround the core – all of which are made of Haynes 230, a nickel-chromium-tungsten-molybdenum alloy designed for use in aerospace and energy industries [7] [2]. In its simulations, this project will directly replace Haynes 230 with the candidate claddings to perform a parametric analysis.

It is understood that Haynes 230 may have been chosen for heat pipes and ring clamps for reasons outside the scope of this paper, such as cost, ease of manufacture, or performance in other areas. As such, this analysis will not conclude on whether the candidates are a good fit for Kilopower specifically, rather it will compare their performance in conditions typical of this reactor environment (HEU, micro, etc), using Kilopower as a benchmark.

The reported results of KRUSTY will be used for operational parameters. This means the fuel will generate 5 kW of heat and maintain an average temperature of 800 C. Two-phase Sodium coolant will be simulated through the heat pipes, with inlet and outlet temperatures based on the Stirling converter cold and hot ends of 70 C and 660 C. The core will be in a vacuum, instead of air, and surrounded by a BeO shield [15].

This work is designed to be as accurate to the conditions expected in this reactor environment as is reasonably necessary. Certain factors have been approximated or cut for expediency because the impacts on the results are deemed negligible or outside this project's scope. These will be noted throughout the paper.

2.2. CANDIDATE CLADDINGS

Because of their low thermal neutron absorption cross section and resistance to corrosion, Zirconium-based claddings have been the main choice for uranium fuel pellets in LWRs since the 1950s [8]. Of these, as one of the most common Zr alloys, Zircaloy-4 was chosen for this project. The only difference with the other common alloy, Zircaloy-2, is that it is three times more resistant to the production of hydrides, which will not be relevant to this analysis [18]. Although it is not designated an ATC, Zircaloy-4 will provide a baseline for the other candidates. And because it is designed for LWRs, its performance in a non-LWR will still be of interest.

Iron-based nuclear claddings have been in use since 1951, where austenitic stainless steel was deployed in the Experimental Breeder Reactor I. Survey tests of Fe-based alloys found the high temperature oxidation resistance of FeCr, FeAl, and FeCrAl made them desirable. Of these, FeCrAl was chosen to move forward and has undergone significant testing. Normal operational and anticipated operational occurrence behavior are expected to be superior to Zr-based cladding, but based mainly on its enhanced oxidation resistance [8]. FeCrAl will be one of the candidate claddings.

Silicon Carbide (SiC)'s use in the nuclear industry reaches far back, but high-strength fiber-reinforced composites (SiC-SiC, as opposed to bulk SiC) date to research in the 1970s. The technology for its production has improved since and owing to its exceptional oxidation resistance, it is likewise deemed an ideal accident tolerant cladding [8]. Its status as a ceramic also lends itself to different material behaviors from metals, which may prove interesting for this analysis. For instance, it does not have a known melting point, rather a sublimation point and low plastic deformability means mechanical failure is more likely to result from surpassing flexural strength limits, as opposed to yield strength limits [19] [20]. SiC-SiC will thus be another candidate cladding.

Haynes 230, the original choice for the heat pipes and ring clamps, will be included in the simulations as another baseline for KRUSTY benchmarking.

Table 2.1. Candidate Cladding Material Properties

	Haynes 230 [7]	Zircaloy-4 [21]	SiC-SiC [22] [19]	FeCrAl [23] [4]
Young's Modulus (GPa)	159	99.3	240	135
Poisson's Ratio	0.34	0.37	0.191	0.3
Thermal Expansion Coefficient ($1/K$)	15.2e-6	6e-6	5.5e-6	13.4e-6
Thermal Conductivity ($W/m*K$)	24.4	21.5	68.85	22
Specific Heat Capacity ($J/kg*K$)	595	285	1200	710
Density (kg/m^3)	8970	6550	2700	7150
Melting / Subl. Point (K)	1574	2123	2700	1773

The oxidation resistance of these candidates will not be relevant to this analysis. Rather, it is their thermodynamic and mechanical behaviors that will be examined. For instance, SiC-SiC has displayed notable stability under irradiation and fracture toughness, but does not allow for significant creep before failure [20].

The properties used for the four candidates are compiled in Table 2.1. Also included is melting point / sublimation point (for SiC-SiC), a common failure limit for the candidates for their performance to be measured against. Although not a candidate cladding, the maximum temperature of the U8Mo fuel will be compared against its melting point, 1408 K, as another performance metric [24].

$$Variable\ Fraction = \frac{Maximum\ Measure\ of\ Variable}{Limit\ of\ Variable} \tag{2.1}$$

Another failure limit, yield strength (YS) / flexural strength (FS) (for SiC-SiC), is plotted against temperature in Figure 2.1. If temperatures exceed the limits of this data, the closest datapoint will simply be used (so 1800 K FeCrAl would use 30 MPa, the same as 1100 K FeCrAl). This failure analysis will be further elaborated on in Section 4. The measurement for any failure limit will take the form of their 'fraction', Equation 2.1, each named after the environment, component, and operating variable. For instance, a comparison of maximum fuel temperature and fuel melting point during NOC would be the 'NOC fuel temperature fraction.'

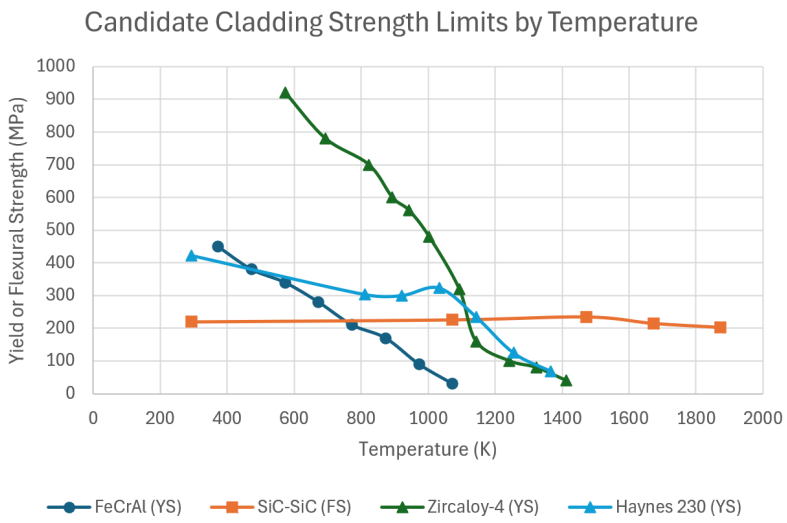

Figure 2.1. Yield strength (YS) or flexural strength (FS) for each candidate cladding [4] [5] [6] [7].

2.3. MULTI-PHYSICS SOFTWARE AND APPROACH

The analysis done on Kilopower will be multi-physics, meaning multiple fields of modeling and simulation (M&S) will be used and coupled together, with the goal of providing more holistic results. In this case, neutron transport, heat transfer, thermodynamics, and continuum mechanics. This approach provides a through line to arrive at the desired results: performance and failure modes of the candidate claddings, based on measure of temperature and stress levels they experience.

The following is a brief overview of the M&S efforts, illustrated visually in Figure 2.2. More detail will be given in each relevant section, from 3-5. Since the results of one software determined the approach to the next, this was deemed the most effective way to break down the project.

Monte Carlo N-Particle Transport (MCNP) is a probabilistic software developed by Los Alamos National Laboratory (LANL) and designed to track simulated particles through user-defined geometry [25]. It has the capability to simulate complex geometries

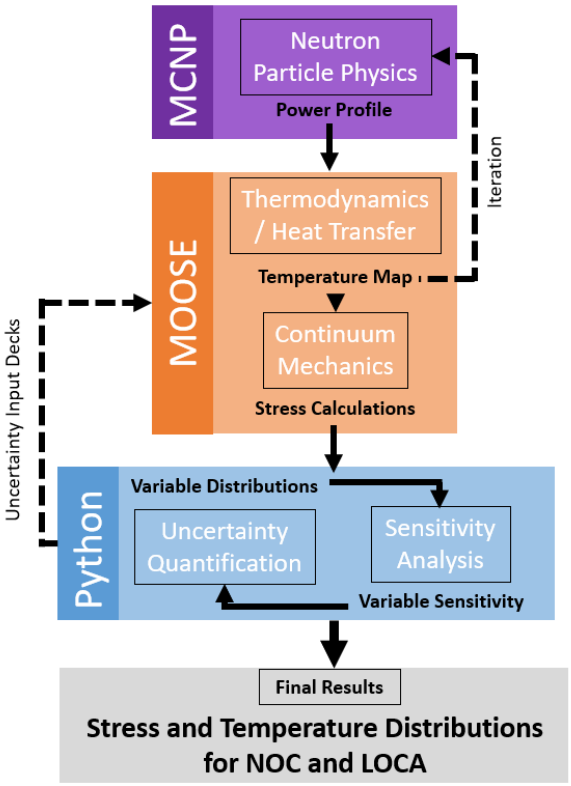

Figure 2.2. The combined M&S approach to model Kilopower performance and failure modes.

with sufficient customization to replicate the Kilopower reactor. It will be run remotely on The Foundry, Missouri University of Science & Technology (S&T)'s High Performance Computing (HPC) cluster [26].

The M&S effort begins here, because any knowledge gained from a thermodynamic / heat transfer model is predicted to not affect the neutronics of the MCNP model (and thus the power peaking calculations) in a significant way. Should it do so, this software can be run again with updated temperatures and continuously iterated on until the most accurate results are found.

Specifically, the power profile of the Kilopower fuel will be measured, using fission rate in different axes - axially, radially. While the core has a total thermal power rating, knowing which areas have the highest heat density create a more accurate map of the core's temperatures in the next step.

Multiphysics Object Oriented Simulation Environment (MOOSE) is a finite element framework developed by the Idaho National Laboratory (INL), used by this project for its heat transfer and continuum mechanics capabilities. It will be run remotely on the Nuclear Science User Facility HPC cluster at INL [27].

MOOSE provides the necessary tools to perform thermodynamic, heat transfer, and continuum mechanics analysis all-together. The different modules that are loaded within interact with one another, forming a multiphysics framework in and of itself. Heat generation in the fuel combined with effects of the coolant will form a temperature map. That map informs thermal expansion, causing displacement, which is used to calculate stress and strain that the geometry experiences. The temperatures and stresses measured here are the main results used for this analysis. But they will also form a baseline for the next step.

Although the results from MOOSE say much about the candidate claddings' performance, there is more analysis that can be done with the model. All M&S have inherent uncertainty, originating from either unforeseen errors in the simulation (aleatoric) or inaccuracies in the model's setup, such as boundary conditions or other assumptions (epistemic). This project will account for epistemic uncertainty in some candidate material properties using uncertainty quantification (UQ) and the effects of that variance on results will be measured with sensitivity analysis (SA). This will be done via the coding language Python, notably the packages *chaospy* and *pandas* for their abilities to generate / sample distributions and read large volumes of data (specifically *csv* files) respectively.

The method chosen is non-intrusive Polynomial Chaos Expansion (PCE), which is sampling-based and data-driven. 'Non-intrusive' means it does not require modification of the base M&S to be performed. In this method, choice input variables of the model are

assigned uncertainties, expressed as probability distributions. These inputs and all model outputs are represented by orthogonal polynomial coefficients of the PCE and can be used to compute statistical moments (such as mean and standard deviation) for the outputs using projection, regression, or collocation.

Use of UQ and SA are recent trends in engineering [28] [29]. They allow for even the most simple of M&S efforts to still measure and account for variance in either the data being used or results generated [20]. This project will use them to investigate how sensitive the MOOSE model's results are to uncertainty in some candidate claddings' material properties, by running it in large input decks. A distribution will be created based on that sensitivity. If, for instance, a 5% uncertainty in a property causes the component to have a 40% chance of failure, the recommendation will be for future experimental work on that material to clarify the exact property value. If the chance of failure for another candidate is only 2%, it will be less of a priority. These are the final results of the analysis.

3. MCNP

3.1. PARTICLE TRANSPORT AND POWER PRODUCTION

MCNP is a stochastic particle transport code, meaning it relies on large amounts of simulated collisions to dictate where particles will travel. These collisions depend on isotopic cross sections, defined by materials assigned to the user-defined model geometry. Particles move in a straight line between collisions, which are governed by randomly sampled probabilities that influence its next direction [25]. An example of a particle transport is in Figure 3.1, where a neutron's interactions cause several other particles to be spawned and then subsequently tracked.

Its stochastic nature means that it uses an arbitrary number of particles to 'map' out the probability each will reach and / or interact with locations in tallies, calculated with Equation 3.1:

$$\overline{\phi_V} = \frac{1}{V} \int dE \int dt \int dV \int d\Omega \, \Psi(\overrightarrow{r}, \Omega, E, t) \tag{3.1}$$

V is tally volume (cm^3), E is particle energy (MeV), t is the time (shakes; 1 sh = $10^{-8}s$), Ω is the particle direction unit vector, $\overrightarrow{r}$ is the particle position vector (cm), and Ψ is the angular flux as typically defined in nuclear reactor theory ($\frac{Particles}{cm^2 * sh * MeV * steradian}$) [30]. The tally counts $\overline{\phi_V}$ are output as 'source-averaged,' meaning an area with, for example, 10% of all source particles would have a particle fluence of 0.1 $\frac{Particles}{Source\ Particles * cm^2}$ [25]. It also means that instead of needing to simulate the infeasible amount of *actual* particles in a reactor, one may take these probabilities and properly scale them by calculating the total amount of particles within the model environment and applying that to the probability map [31]. That scaling will not be necessary for this analysis, but it is worthwhile to clarify.

In the case of nuclear reactors, the particle of interest is the neutron. Neutrons cause fissioning of fissile materials, which not only release energy but also release more neutrons, leading to a chain reaction. It is the control or moderation of neutron production

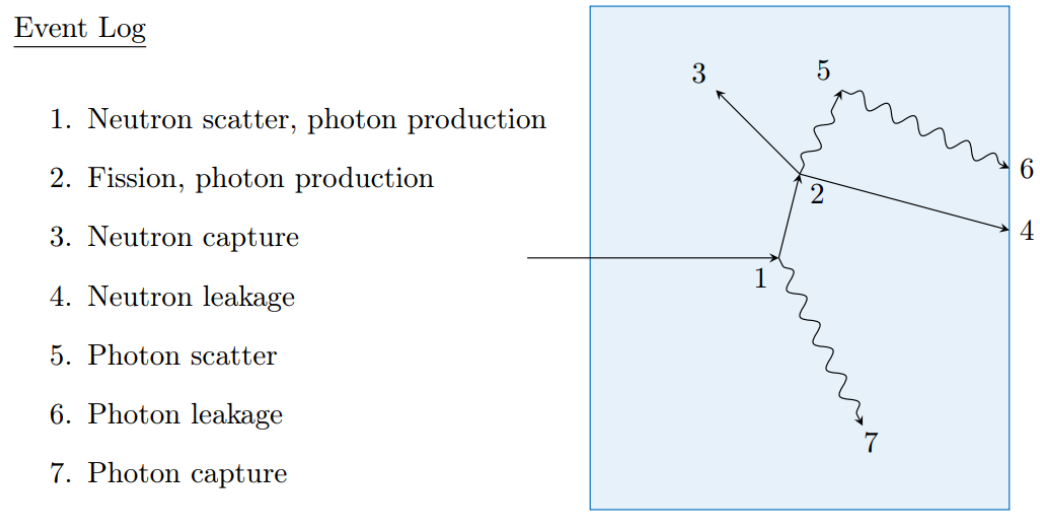

Figure 3.1. Various particle random walks. The zigzag lines are used to represent the moving of photons in the MCNP user manual, but the MCNP code treats a photon movement as a straight line between collisions[25].

that controls power generation within a reactor. Applying cross section data to particle tallies, MCNP can measure the rate at which neutrons collide with fissile isotopes (in this case ^{235}U) and cause fission ($\frac{Fissions}{Source\ Particles*cm^2}$). This fission rate is proportional to power production in the reactor and will be used to calculate heat generation rate (power profile) across the fuel [31].

The MCNP input script was generated in Python using simple read and write functionality for *.txt* files. This allowed for quick changes to be made to specific variables at the top level, like the material composition for the ring clamps and heat pipes. This was particularly useful for investigating if the cladding candidates' isotopic compositions would affect the neutron spectrum within the fuel and thus impact power shape.

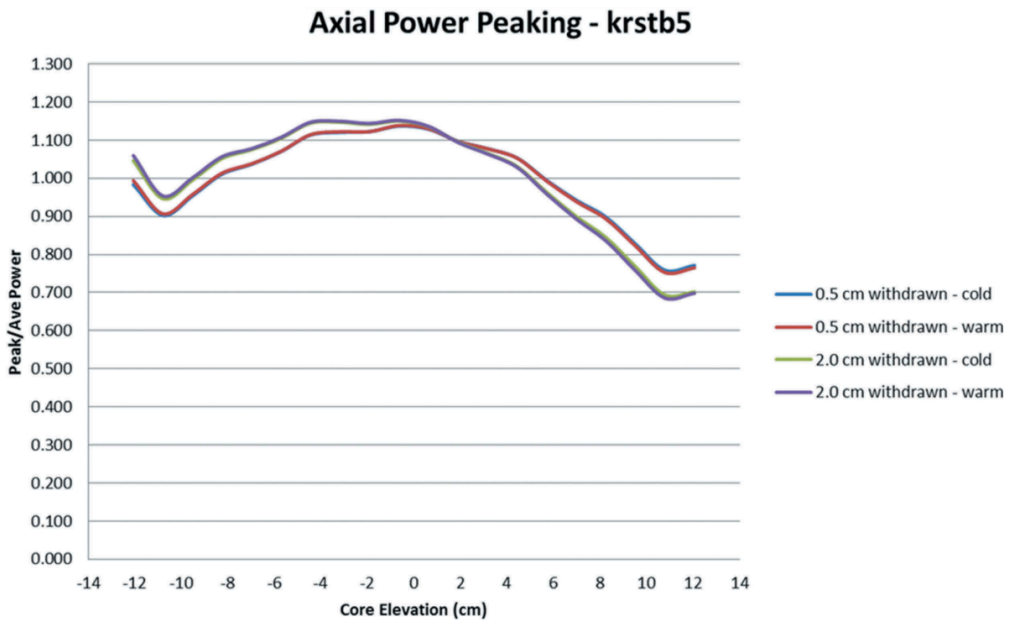

Figure 3.2. Axial power peaking in KRUSTY fuel, measured by the Kilopower team's MCNP script, depending on control rod height and temperature [2].

Calculating axial power profile (APP) from fission rate involved converting to a unitless representation of power shape. To find this shape, each axial fission rate was divided by the average fission rate across the axial length of the core. Because this step's main purpose was to use that APP to create a heat generation formula to be used in MOOSE, benchmarking from the Kilopower results were sought out for comparison.

3.2. KRUSTY MODEL AND POWER PEAKING

Figure 3.2 shows a gradual curve over the fuel's length. Outliers are at the top and bottom edges and were not noted by the Kilopower team. They are likely caused by the BeO shielding moderating any escaping neutrons and reflecting them back inside the core, where they are now more likely to cause fission. Five crests over the length are from the gaps between the ring clamps, similarly allowing more moderated neutrons to enter the fuel. These represent only a 1% deviation and were deemed by the Kilopower team as negligible.

Thus, to create an APP that will be easier to generate a function from, these peaks were not be accounted for in this project. The ring clamps in the MCNP geometry were combined into a singular ring clamp.

There was noticeable difference in the APP depending on control rod height. This analysis will neglect the control rod and impact on power peaking for simplicity and equity between runs, with the assumption that the reactor is operating at full power in all scenarios and that the relative position will not affect the ultimate performance or failure metrics in a significant way.

Kilopower's sodium coolant is two-phase, so the material was written to be particularly modular with its density, allowing it to represent any mixture of liquid and vapor sodium. To investigate the potential effects of sodium coolant phase composition on the power profile, two runs would be done, one with completely liquid sodium (0.971 g/cm^3) and one with completely vaporous sodium (0.060 g/cm^3). Up until then, all runs would be done with liquid sodium.

Taking baseline temperatures and material properties (density and isotopic composition), the Kilopower core and surrounding geometry were constructed. The model was based on the KRUSTY configuration, as in Figure 1.3. Due to the purpose of the reflector (to retain neutrons within the core), it was deemed a boundary where no particles that escaped it would be relevant, so no geometry outside of it was rendered. Particles beyond this boundary were 'killed,' meaning their further transport was no longer tracked. The entirety of the rendered geometry can be seen in Figure 3.3.

Because Kilopower's cylindrical fuel is homogenous, it was anticipated that during NOC, fission would only vary axially, as opposed to angularly or radially. Fission rate would be captured axially in forty 0.625 cm axially-long cylindrical bins. To test the latter assumption, a 2D mesh across the radial-angular plane, divided into 0.1 cm x 0.1 cm bins, measured the Kilopower fission rate.

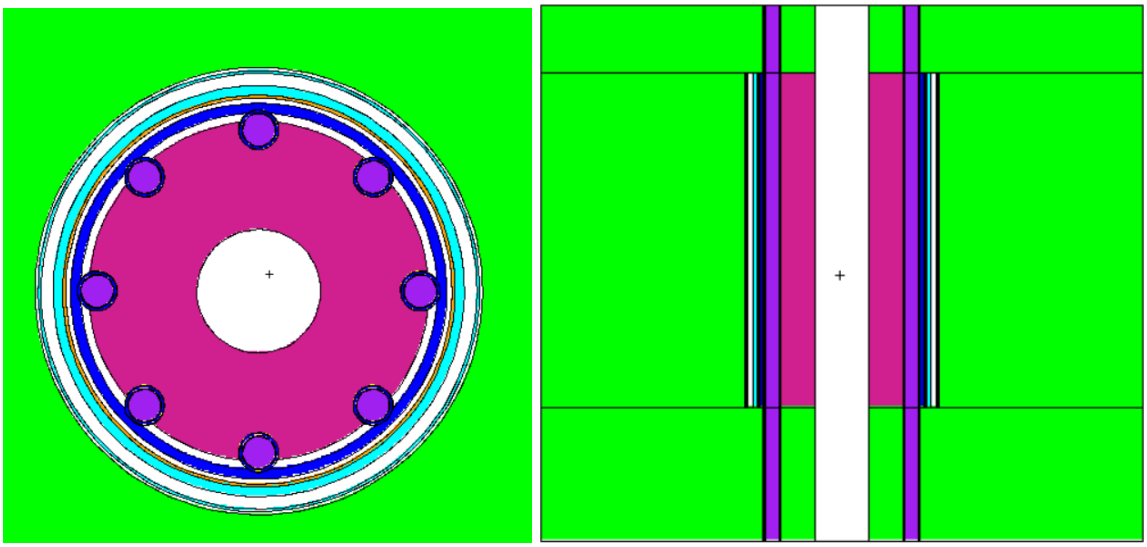

Figure 3.3. KRUSTY core recreated in MCNP, viewed at the radial-angular and radial-axial planes. From inner to outer, the central layers are fuel (fuchsia), singular ring clamp (blue), MLI (orange), vacuum can and steel sleeve (teal), and BeO shield (green). White represents void / a vacuum. The eight heat pipes (blue) are filled with a customizable Sodium material (purple) and have inner nickel wick and outer copper foil layers (unseen).

3.3. MCNP RESULTS AND DISCUSSION

In Figure 3.4 it is shown that, angularly and radially, the fission rate is constant - except for minor peaks at the outer edges, likely due to more moderated neutrons being reflected back from the BeO shield. Like the Kilopower team's data (Figure 3.2), the axial profile also saw peaks at the top and bottom edges. Power peaking in the fuel's axial center was expected due to the larger concentrations of neutrons being released from fission in other parts of the fuel. And as anticipated, turning the six clamps into a singular ring clamp eliminated the five minor power peaks in between each clamp.

Because the peaks at the edges represented such a thin margin of either power profile, these datapoints were deemed insignificant enough to be removed before performing linear regression. To reiterate, this project seeks to recreate comparable conditions in this type of microreactor, not recreate Kilopower or KRUSTY one-for-one. And even the Kilopower team deemed such peaks to be insignificant to heat transfer calculations [2]

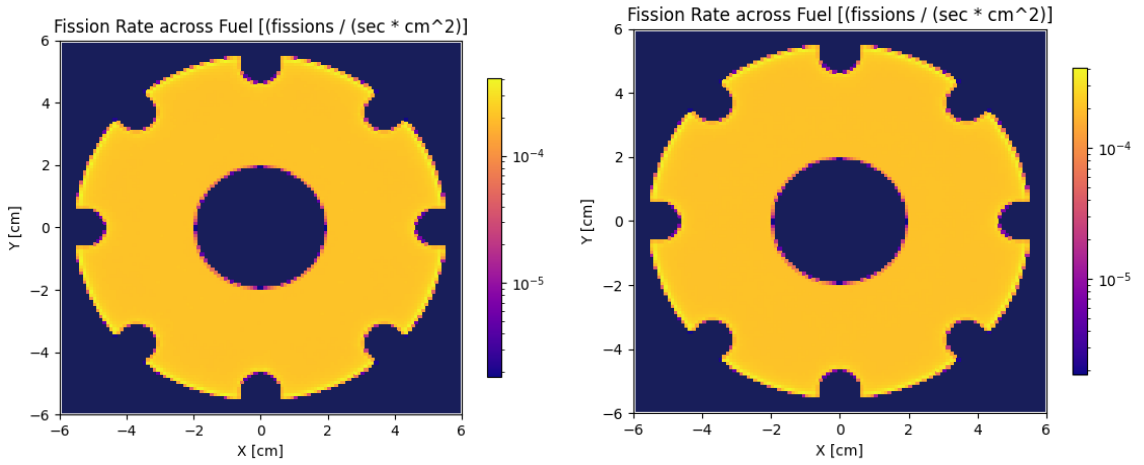

Figure 3.4. Fission rate (source-averaged) across the entire axial length of the Kilopower fuel, viewed in the angular-radial plane. The first graph experiences NOC. In the second graph, a LOCA has occurred in the rightmost heat pipe. There is no significant difference in angular or radial fission rate, both for and between NOC or LOCA conditions.

Overall, the behavior is very similar to the Kilopower benchmarking with 2.0 cm withdrawn in Figure 3.2, taken by this project as a green light for the MCNP model's veracity.

Further runs investigated the impacts of liquid vs vapor sodium coolant, heat pipe / ring clamp cladding choice, and NOC vs LOCA conditions on the APP. The results are in Figure 3.5. Although the source-averaged fission rates differ by a small margin, once the results are divided by their average, it can be seen that the power profile shape is nearly identical in all cases (Fig. 3.6). The difference in overall fission rate would imply that the cases have different overall thermal power ratings - however, in practice, all of the different scenarios would be kept at the same thermal power (5 kW) through adjustments of the control rod or coolant flow. This was enough justification for the variations of the subsequent thermodynamic model to use the same power profile, as opposed to a different profile for each starting condition.

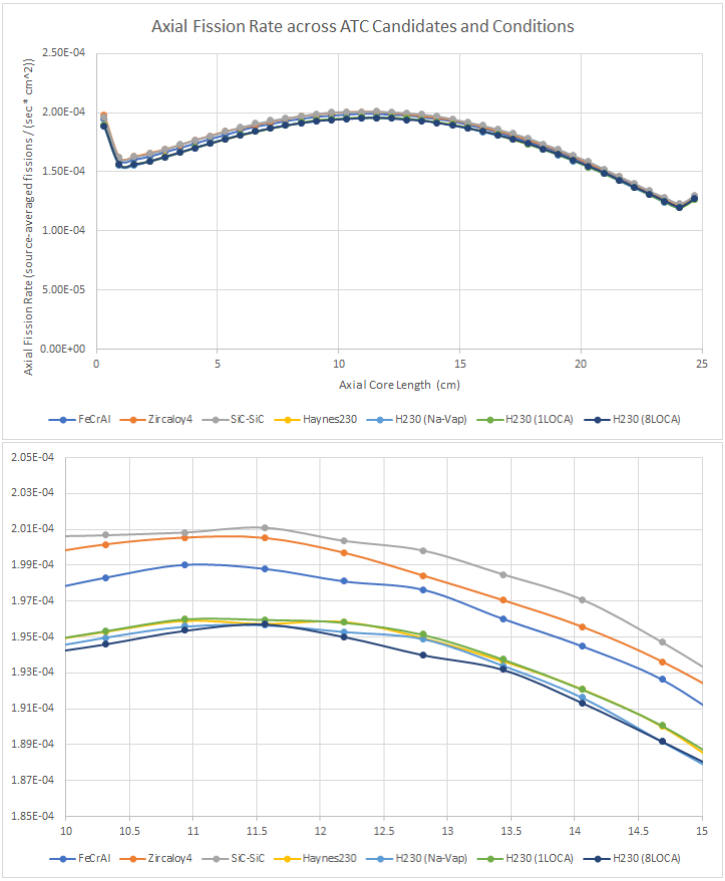

Figure 3.5. Axial fission rate (source-averaged) of the Kilopower fuel block - both the entire core and magnified for clarity.

Equation 3.2 is the APP of the Kilopower fuel, drawn from Figure 3.7. Its range is from 0 to 0.25 cm and will be multiplied by Power Density in the MOOSE model. The radial and angular profiles need only be represented by a constant of 1.

$$APP = -27.626 * z^2 + 6.1654 * z + 0.8048 \tag{3.2}$$

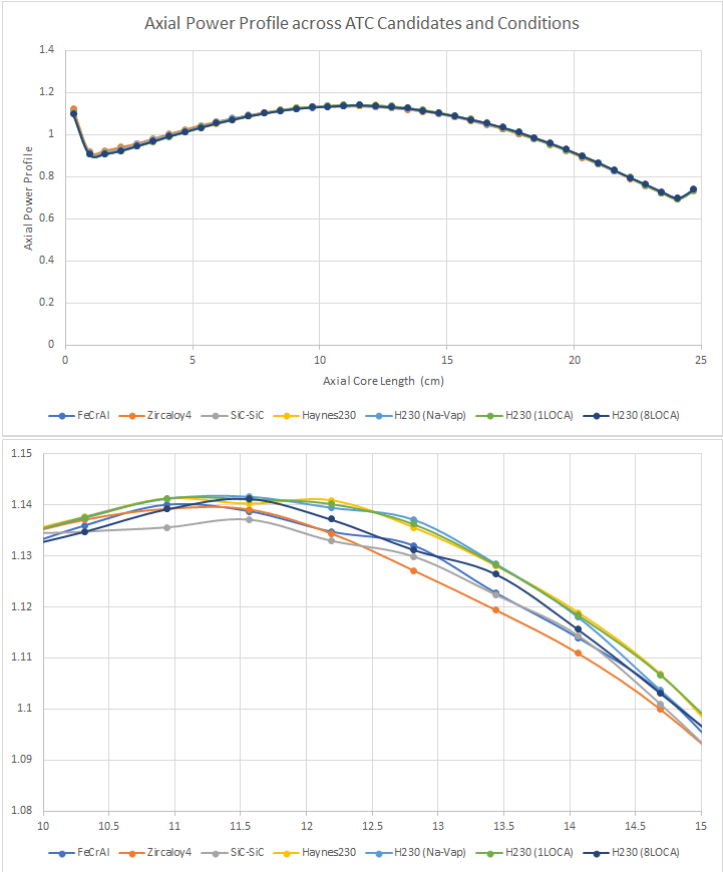

Figure 3.6. Axial power peaking of the Kilopower fuel block - both the entire core and magnified for clarity.

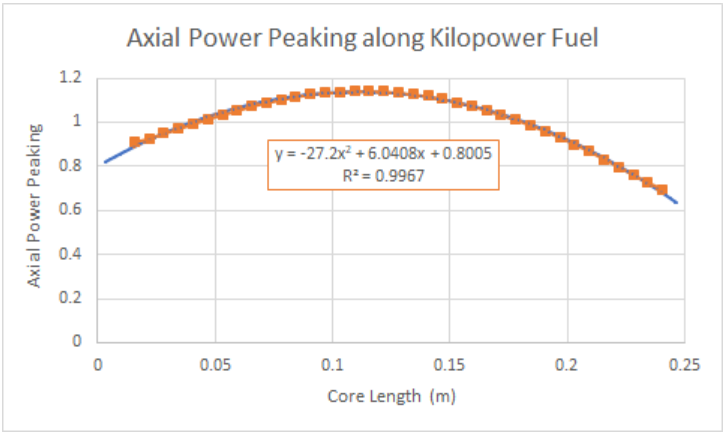

Figure 3.7. APP of the entire Kilopower fuel block (orange) and the extrapolated equation to represent it (blue).

4. MOOSE

Unlike in particle transport calculations, it is typically unnecessary to model a significant portion of a system in finite element analysis. Where symmetry can be found, computations can be saved by assuming what occurs across from the symmetrical boundary is a mirror of the model. The cylindrical nature of the Kilopower core allowed symmetry to be found between its eight heat pipes.

Thus for simplicity of the computations, a 1/8 angular slice of the Kilopower core was modeled and meshed (Figures 4.1 and 4.2), with only the components most relevant to the calculations: fuel, heat pipes (with Ni and Cu layers), and ring clamps. This was done in Gmsh, an open-source, text-based finite element mesh-generator [32]. Gmsh accounted for the definition of geometry, surfaces, and volumes and subsequent 3D meshing definitions, such as element resolution and block definition. The core's axial direction is interpreted as the mesh's Z axis, with radial and angular directions defined across the X-Y plane. The mesh was exported as a native *.msh* file. This was read by a separate MOOSE script and converted into MOOSE's default *.exd* (Exodus II) mesh file format, ready to be used by the MOOSE M&S input.

This early model modified the axial lengths of the clamps and their gaps so the meshing would be more uniform (2.679 *cm* and 1.786 *cm* vs the actual 2.72840 *cm* and 1.72592 *cm*). The core was also lengthened slightly (25.004 *cm* vs the actual 25 *cm*). All-together, this allowed for a uniform mesh resolution of 28 elements across the axial direction. This was anticipated to not have a significant effect on the results. And all three heat pipe layers were separated into four angular sections to better allow mesh-sizing definition, based on which surface (or lack therof) was adjacent to the pipe.

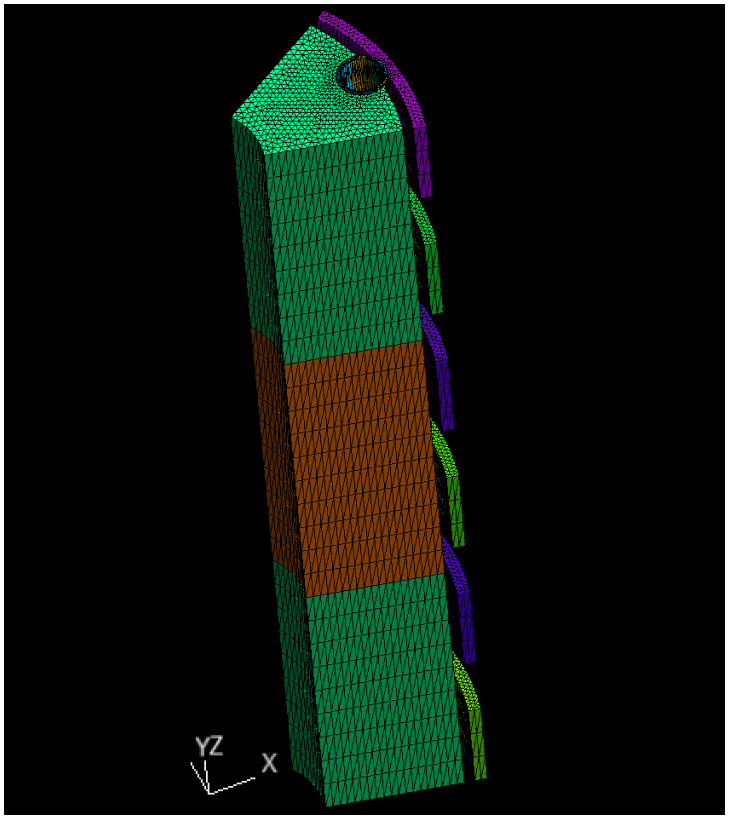

Figure 4.1. 1/8 section of the Kilopower core (fuel, heat pipe, ring clamps) viewed from the X, Y, and Z axes.

4.1. HEAT CONDUCTION AND THERMODYNAMICS

4.1.1. MOOSE Heat Transfer Module. In this 1/8 Kilopower model, the power shape from MCNP informed heat generation within the MOOSE fuel block, by being multiplied against power density $\dot{P}$. With a steady-state power P of 5 kW, the project only needed to solve for the fuel block's volume to find power density. The fuel block was a relatively complex shape to solve for - thankfully, the Kilopower team reported a fuel mass density ρ_F of 17,340 $\frac{kg}{m^3}$ and total mass m_F of 32.20 kg [2].

$$\dot{P} = \frac{P * \rho_F}{m_F} \tag{4.1}$$

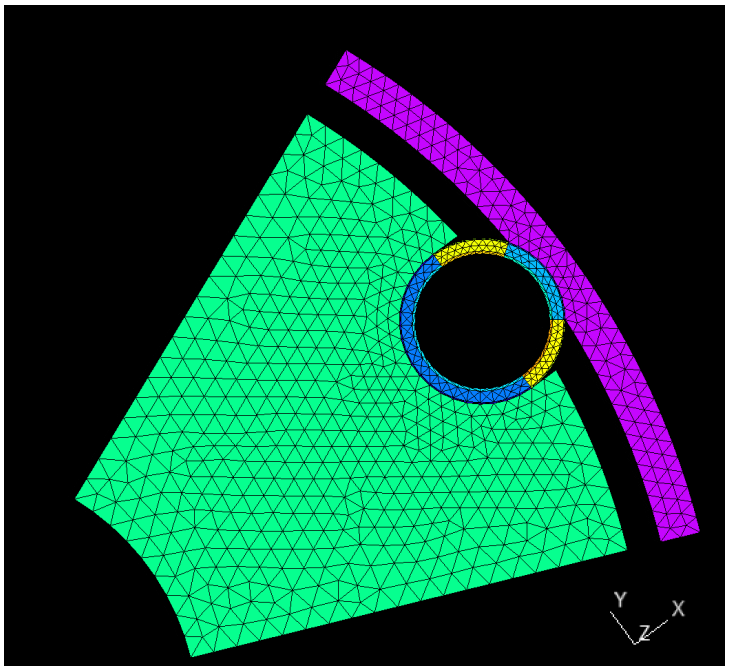

Figure 4.2. 1/8 section of the Kilopower core (fuel, heat pipe, ring clamps) viewed from the X and Y axes.

4.1.2. Sodium Coolant Simulation. Many ways to simulate the interaction between the fuel's internal heat generation and coolant (Na vapor) along the boundaries of the heat pipe interior were investigated. Initially, the Thermal Hydraulics Module was used. The 3D mesh was imported as a heat structure and a 1D flow was simulated along the pipe interior. However, the Thermal Hydraulics Module is not compatible with the Tensor Mechanics module (which was needed to calculate stress), so this approach was shelved. Instead, the Heat Transfer module would simulate temperature interactions of the mesh.

This module's basic theory follows the heat conduction equation:

$$\rho(t,\overrightarrow{x})c(t,\overrightarrow{x})\frac{\delta T}{\delta t} = \nabla k(t,\overrightarrow{x})\nabla T + \dot{q} \text{ for } x \in \Omega \tag{4.2}$$

where T is temperature (K), t is time (sec), $\overrightarrow{x}$ is the vector of spatial coordinates (m), ρ is the density ($\frac{kg}{m^3}$), c is the specific heat capacity ($\frac{J}{kg*K}$), k is the thermal conductivity ($\frac{kg*m}{sec^3*K}$), $\dot{q}$ is a heat source ($\frac{J}{sec}$ or $Watts$), and Ω is the domain (m) [33]. Within the software, no units are directly assigned to any properties or variables, as they are dependent on the user-defined values given. All of the units given in this section are what was chosen by the project.

The question then became how to best simulate the coolant. BISON, a finite element code built off MOOSE, was available to the project and includes a Coolant Channel system built specifically for this purpose [34]. However, it was built around simulating common parameters in the nuclear industry and did not allow for the freedom this project required. For instance, the model needed to simulate two-phase Sodium, and the Coolant Channel system only allowed for liquid Sodium.

Directly modeling the coolant was another option. A version of the mesh was created with the coolant as a new 3D block (Figure 4.3). However, the limit in this case was the benchmarking. Not enough information on two-phase properties of sodium could be found (coolant velocity, quality), either from the KRUSTY results or other sources, to the degree of detail that was needed. Additionally, this would've greatly increased the model complexity. Since the goal of this project was only to simulate the effects of the sodium on its surrounding components and not the sodium itself, this was likewise shelved.

A simple boundary condition (BC) of convective heat transfer was settled on. In MOOSE, BCs are defined on the boundary of the domain, $\delta\Omega$. These are divided into Dirichlet BCs $\delta\Omega_D$ and Robin BCs $\delta\Omega_R$, such that $\delta\Omega = \delta\Omega_D \cup \delta\Omega_R$:

$$T(t, \overrightarrow{x}) = T_D(t, \overrightarrow{x}) \text{ for } \overrightarrow{x} \in \delta\Omega_R \tag{4.3}$$

$$-k\overrightarrow{n} * \nabla T - G(t, \overrightarrow{x}, T) = 0 \text{ for } \overrightarrow{x} \in \delta\Omega_D \tag{4.4}$$

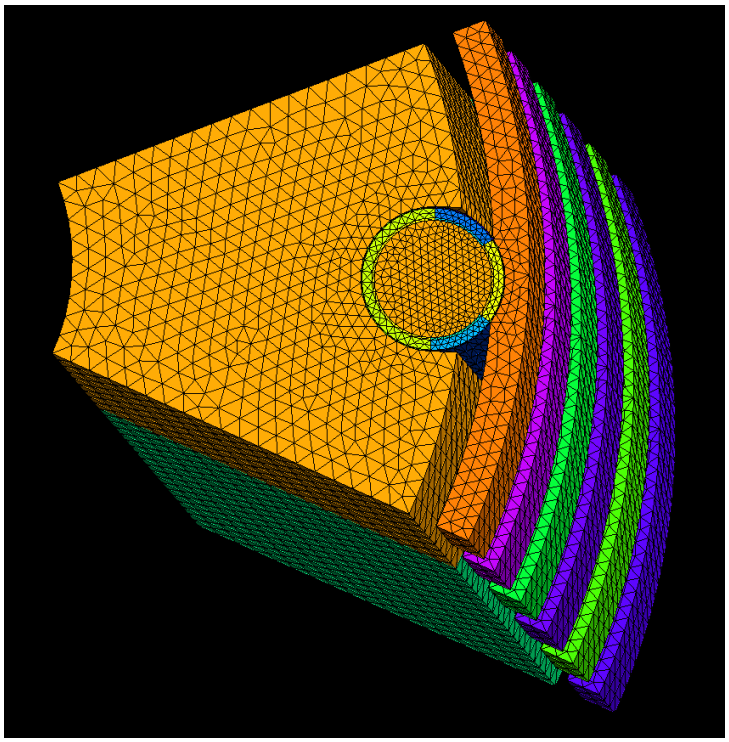

Figure 4.3. Version of the 1/8 Kilopower core slice with 3D-modeled Sodium coolant. This was not used due to the unnecessary complexity being added to the model's input definitions and computational cost.

T_D and $G(t, \overrightarrow{x}, T)$ are known functions $\overrightarrow{n}$ is the outward normal of $\overrightarrow{x}$. The function $G(t, \overrightarrow{x}, T)$ defines Robin BCs, such as the convection case used for the sodium coolant:

$$G(t, \overrightarrow{x}, T) = h(T - T_\infty) \tag{4.5}$$

where h is the heat transfer coefficient ($\frac{W}{m^2 * sec}$) and T_∞ is the temperature of the surroundings (K) [33]. As this is two-phase convection, the T_∞ of the fluid is irrelevant, as it is the phase change from vapor to liquid that causes heat transfer along the heat pipe walls. Thus, T and T_∞ are combined into δT. With that, Newton's Law of Cooling can be used to substitute h and δT for q, the local heat flux density ($\frac{W}{m^2}$),

$$q = h\Delta T \tag{4.6}$$

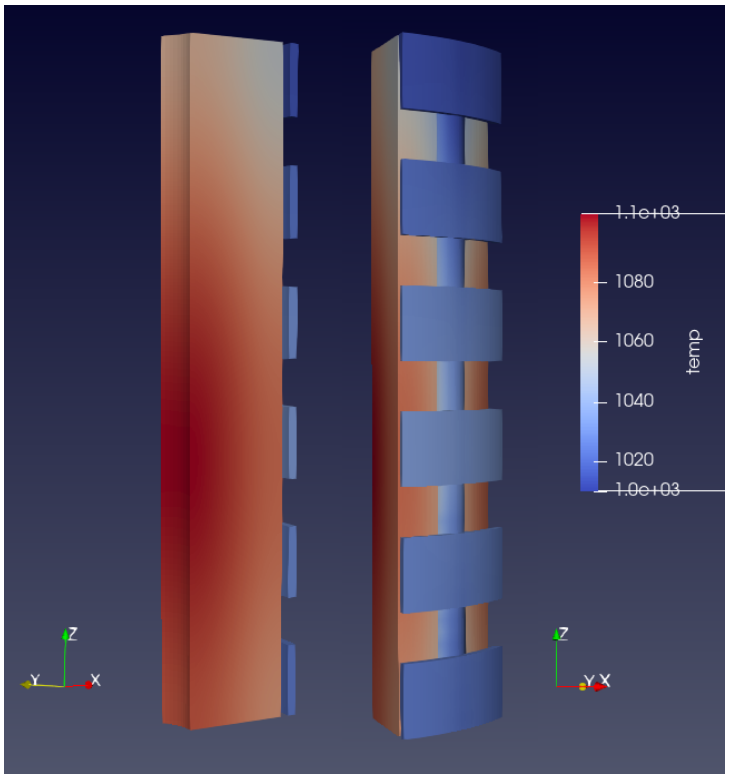

Figure 4.4. Heatmap of the Kilopower model during NOC, viewed at two angles. The average fuel temperature is 1075.36 K.

which was estimated through various iterative simulations until the resulting average fuel temperature fit the ~ 800 $^{\circ}C$ (1073 K) that was reported from KRUSTY [35]. This calculated heat flux is 615,125 $\frac{W}{m^2}$ and resulted in the heatmap of Kilopower in Figure 4.4.

4.2. TENSOR MECHANICS

4.2.1. MOOSE Tensor Mechanics Module. Next came the inclusion of the Tensor Mechanics module. This module allows the output of a plethora of stresses and strain values that can be called upon at will, calculated from the thermal expansion and deformation experienced by the model. The module was loaded for all four materials (U8Mo fuel, ATC candidate ring clamps and heat pipe, Cu foil, and Ni wick), which then had their own elasticity tensors, finite strain / elastic stress, and thermal expansion computed [36].

As previously mentioned, thermal expansion is due to increases in temperature, according to the following governing equation:

$$\epsilon^{thermal} = \alpha * (T - T_{stress_free})\mathbf{I} \tag{4.7}$$

where α is the thermal expansion coefficient ($\frac{1}{K}$), T is the current temperature (K), T_{stress_free} is the stress free temperature (K) - below which all thermal expansion computation is ignored, and $\mathbf{I}$ is the identity matrix [37]. The choice of stress free temperature, like initial temperature, had no impact on the final results.

Declaring the materials as elastic means they do not experience permanent deformation and all elastic strain and elastic stress will ultimately be recoverable, which was an assumption this project deemed acceptable, since the materials would likely only be increasing in temperature and thus experiencing positive expansion and deformation. Elastic stress is calculated from elastic strain $\Delta\epsilon$ and the elasticity tensor C through:

$$\sigma = C\Delta\epsilon \tag{4.8}$$

[38]. The elasticity tensor is built from two of five user-provided elastic constants:

$$C^{isotropic} = \begin{bmatrix} \lambda + 2\mu & \lambda & \lambda & 0 & 0 & 0 \\ \lambda & \lambda + 2\mu & \lambda & 0 & 0 & 0 \\ \lambda & \lambda & \lambda + 2\mu & 0 & 0 & 0 \\ 0 & 0 & 0 & \mu & 0 & 0 \\ 0 & 0 & 0 & 0 & \mu & 0 \\ 0 & 0 & 0 & 0 & 0 & \mu \end{bmatrix} \tag{4.9}$$

that being the Lamé parameters lambda λ and shear modulus μ. While it is written using these, Young's Modulus E and Poisson's Ratio ν can be substituted in, with MOOSE internally using the following conversion equations [39] [40]:

$$E = \frac{\mu(3\lambda + 2\mu)}{\lambda + \mu} \tag{4.10}$$

$$\nu = \frac{\lambda}{2(\lambda + \mu)} \tag{4.11}$$

4.2.2. Hoop Stress Analysis. Because the analysis was focused on piping (heat pipes) and pipe-like cylindrical structures (ring clamps), the theory behind this step was based on pipe rupture analysis, where the maximum stress is sought across the FEA model and (should it exceed the failure limits) is the predicted point of failure. The best measurement for pipe rupture is based on hoop stress σ_θ, the measure of internal pressure p acting outwards on a pipe-like structure:

$$\sigma_\theta = p * \frac{d_m}{2d_t} \tag{4.12}$$

where d_t is wall thickness and d_m is mean pipe diameter [41] [42] [41]. The pressure in this case originates from thermal expansion. It can best be illustrated with Figure 4.5. The thin-walled assumption was able to be made because both components, the heat pipes and ring clamps, when at their thickest are still less than 10% their diameter.

In a stress analysis, the areas with the greatest stress are those where the affected area is minimal and affecting force is maximal. It is likely the ring clamps will experience the highest stress levels around the interface between themselves and the heat pipes, where sharp corners can result in high stress concentration factors (SCF) because the affecting force is not being distributed along a smoother surface such as a fillet or arch [41] [43]. These sharp edges were part of the Kilopower design, and while they may result in inordinately high SCFs, they will help this M&S effort to exemplify the differences in the cladding candidates' performance [2]

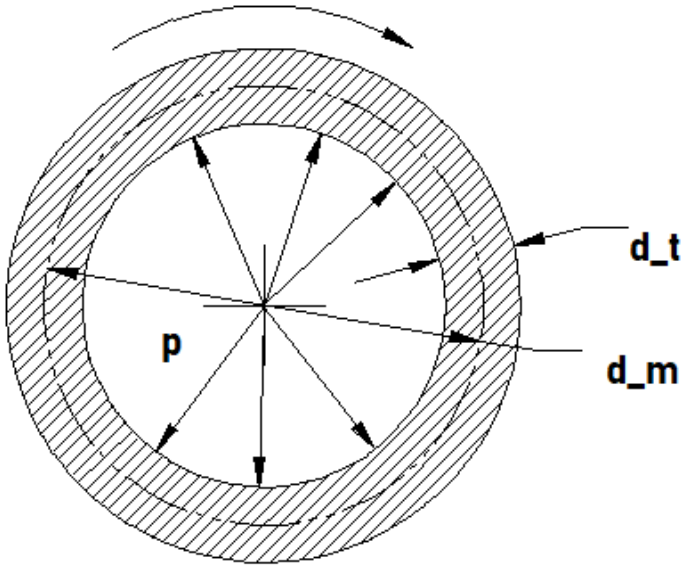

Figure 4.5. Components of hoop stress on a thin-walled pipe. d_t is wall thickness, d_m is mean pipe diameter, and p is internal pressure.

4.2.3. Stress Analysis Difficulties. Much like with simulating the sodium coolant, severe difficulty was encountered while trying to obtain satisfactory hoop stress results. In an ideal scenario, all blocks of the model (fuel, heat pipe, nickel wick, etc.) would be separate and would interact via contact mechanics and contact-based conductive heat transfer. This *was* attempted, but was too computationally expensive to even run. Additionally, MOOSE did not offer contact-based conductive heat transfer - only through the use of gases, such a Helium, could gap-based heat transfer be attempted between two surfaces, and Kilopower operates in a vacuum. Although each block had its own material properties, it would have to be tied to its neighbors, node by node. Since the components being modeled were held together by an interference fit in KRUSTY, this would be accurate in terms of conductive heat transfer being experienced. However, this prevented any slippage between the components - most notably the ring clamps, which could theoretically move in the axial direction. This could result in outlying stresses that skew the results.

To compound the issue, there exists no experimental benchmarking for Kilopower component stresses. The only reliable means of determining accuracy is if the value from the model doesn't exceed the material's own operating limits. Because if it did during testing, there would have been rupture, and it would have been reported - of which no such occurrences were.

As usual, the simplest configuration proved the best means forward. Adjusting what the model was capturing allowed for more accurate BCs, such as preventing angular displacement by halting x-displacement along the Y-axis and y-displacement along the X-axis. This necessitated the model become a quarter slice, instead of an eighth slice. It increased computational costs, but did allow for a more accurate way to simulate a LOCA in one or two pipes and how that would affect other areas of the core with operational coolant. The three heat pipes, in order of clockwise, are designated Heat Pipe 1 (HP1), HP2, and HP3.

Z-displacement along the Z-axis was also prevented, but only along the bottom boundary (coolant outlet, as opposed to the top or coolant inlet). This was necessary to provide the simulation an initial condition for displacement as a whole. Although theoretically, z-displacement along both top and bottom boundaries should be constrained to be accurate to the KRUSTY configuration (where shield blocks would prevent movement in either direction), this was too constrained and produced results that, again, exceeded stress limits during NOC. For the sake of this analysis, it will be assumed that the core has room to expand axially.

Additionally, it was realized that the entire axial length of the core did not need to be modeled. Theoretically, the reactor's hottest portion would experience the most thermal expansion (and thus stress) over any other axial position in the core, during both NOC and LOCA. Thus, when finding the first point that would exceed any stress limits, it was only necessary to model this portion: the hottest ring clamp and the fuel section between both it and the clamp above it, as seen in Figures 4.6, 4.7, and 4.8.

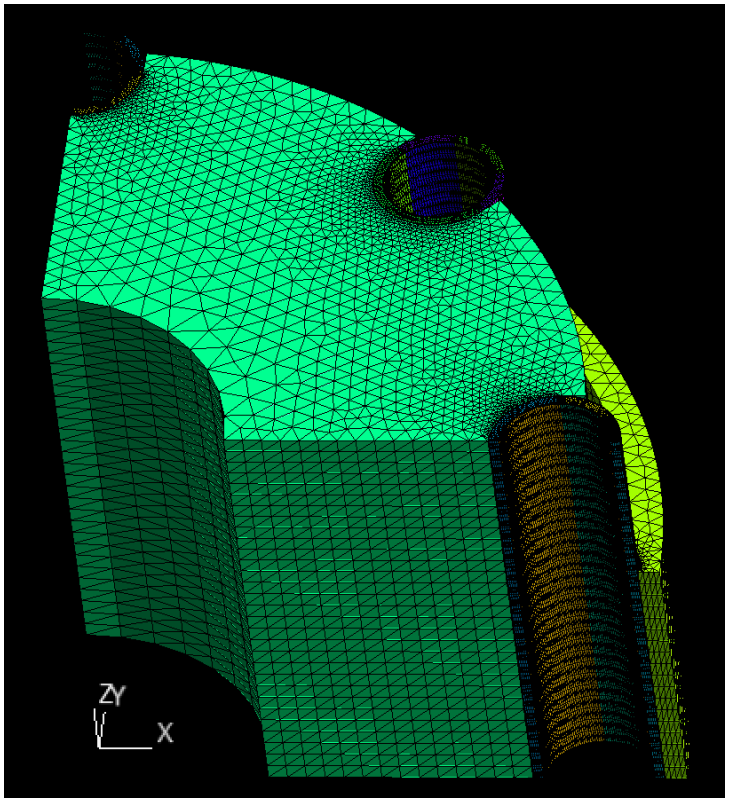

Figure 4.6. 1/4 section of the Kilopower core's RCD (fuel, heat pipe, ring clamps) viewed from the X, Y, and Z axes.

How this was accomplished was through adjusting the axial power profile according to each ring clamp's relative position. From top to bottom the Ring Clamps (RCx) are labeled A-F and were simulated, looking for maximum hoop stress. To account for not having a clamp-less section above it, RCA's model did not include this additional extrusion of the fuel and heat pipes.

Experiencing the highest (Figure 4.10), RCD was chosen (Figure 4.9). This tracks with the highest temperature, fitting the earlier assumption of their positive correlation.

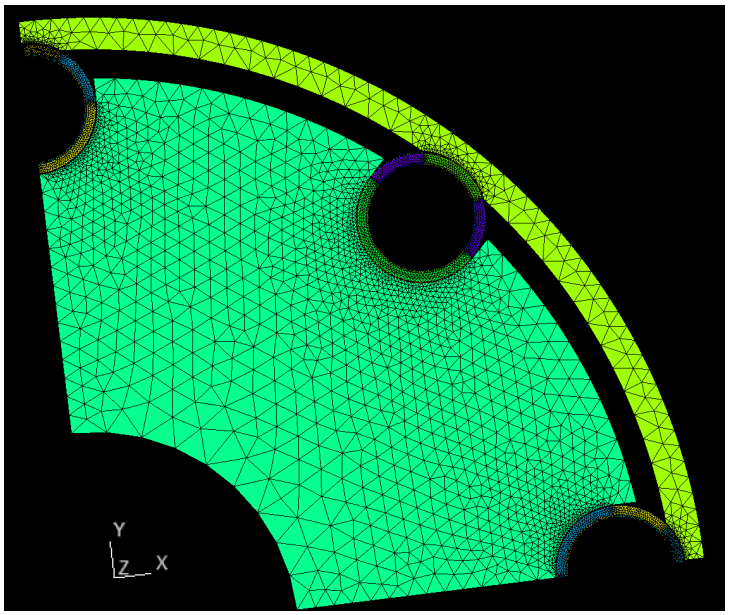

Figure 4.7. 1/4 section of the Kilopower core's RCD (fuel, heat pipe, ring clamps) viewed from the X and Y axes. HP1, HP2, and HP3 are ordered clockwise around the fuel's centerline.

4.3. FINAL MOOSE CONFIGURATION NOTES

Finally, the mesh was refined further along all the heat pipe surfaces. While it increased computational costs, such an expense was deemed worthy of a more robust model. This higher resolution further clarified any potential areas with a high stress concentration factor (SCF), which are areas where the shape of a structure would cause an outlying amount of stress and typically result in failure first [43]. That the heat pipes and surfaces where they interact with the ring clamp are where the stress analysis is focused only further supported this decision.

To swap between the cladding candidates, no changes were needed besides a substitution of the material property values in the MOOSE script (from Table 2.1).

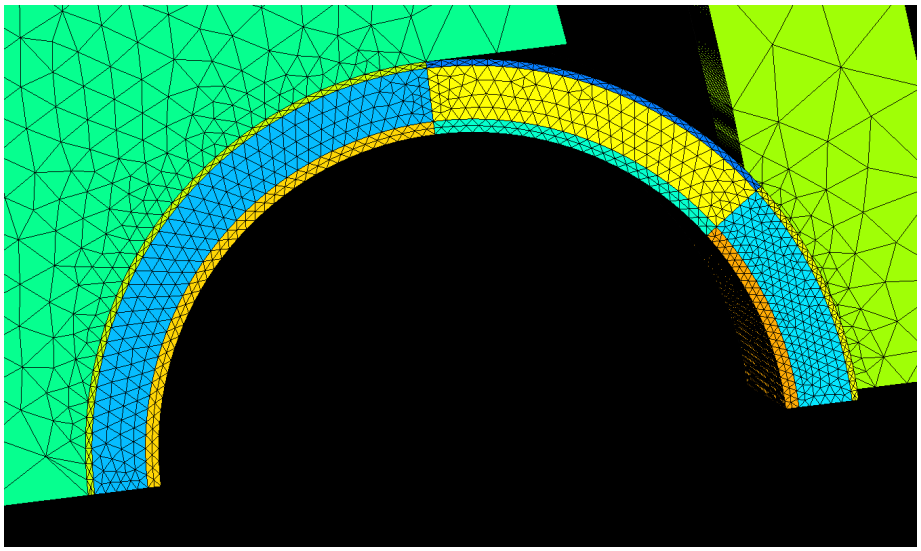

Figure 4.8. 1/4 section of the Kilopower core's RCD, specifically HP3 viewed from the X and Y axes.

4.4. NOC RESULTS AND DISCUSSION

During NOC, all three heat pipes were given the same coolant BC. Although NOC in-concept represent a steady-state system, with no deviations in coolant or power generation over time, it was easier for the solver to converge if the system was designated as transient. All this would mean is that a series of time steps would have to be specified so that, gradually, the solution settled around a set of values for all the variables and outputs. In this case, 'settled' would mean that the differences in results between timesteps are deemed negligible. These results are what the steady-state solver would also have tried to converge around, meaning they should be the same despite the different solver. By the final version of the script, 20,000 seconds was deemed the end timestep necessary to achieve relative convergence.

4.4.1. NOC Exodus Output Model. The resulting finite element model was output in *.exd* format, providing data for each variable / output calculated across all nodes / elements and for every timestep.

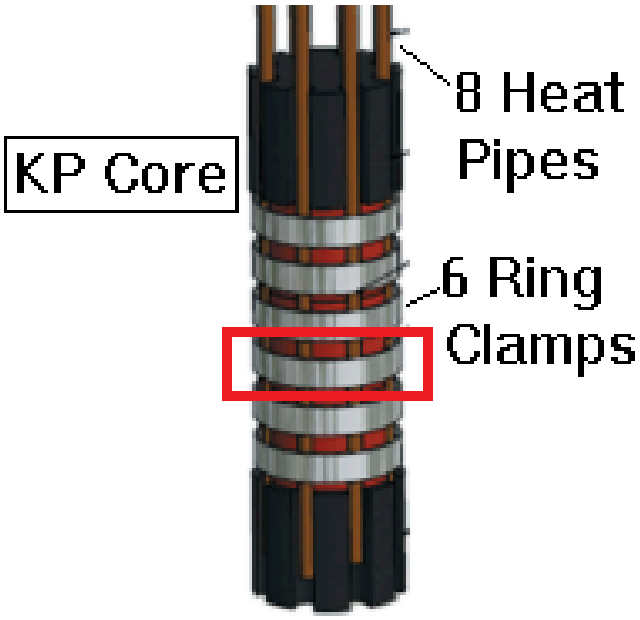

Figure 4.9. Render of Kilopower fuel, heat pipes, and ring clamps. The axial section within the red box is RCD and is what the final MOOSE model captures.

One final reminder, the heat pipes and ring clamps do not directly contact one another - they are separated by a thin layer of copper around the heat pipes. If an interface between the two is mentioned, it is taking that copper into acknowledgement.

The temperature behavior of the model (Figure 4.11) behaves as expected. The fuel center, being the furthest from the coolant and thus experiencing the most heat generation, is the hottest. The ring clamp is essentially 'shielded' by the heat pipes and has a much lower overall temperature than the fuel itself.

As the simulation reaches a steady-state temperature, the model expands. The displacement behavior (Figure 4.12) is near-uniformly positive in all axes. There are small deviations, such as at the ring clamp-heat pipe interfaces, which tracks with the predicted scenario, wherein the heat pipes' own expansion pushes against the ring clamps at these specific interfaces, resulting in more displacement here than in other areas of the ring clamp.

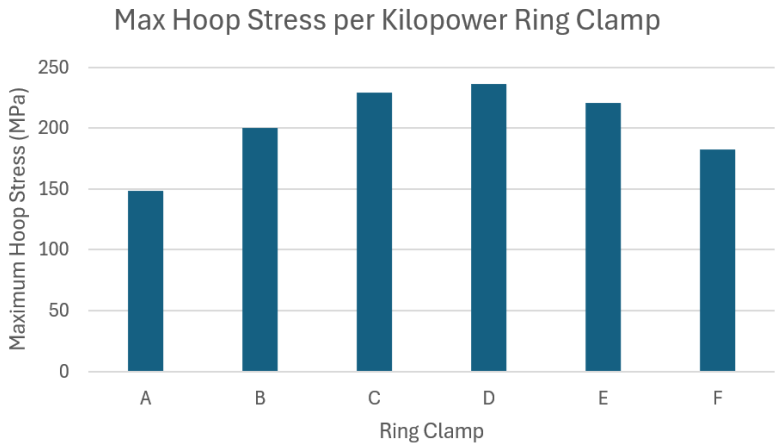

Figure 4.10. The maximum hoop stress experienced by each Kilopower ring clamp model.

That prediction being true was reflected in the hoop stress behavior (Figure 4.13), where the highest stress was found at the heat pipe interfaces and most concentrated near corners (4.14)). The axial edges experience the most negative stress because they are being pushed inward from expansion pushing the interface's center outward. The angular edges experience the most positive stress because at those finite elements, the outward push is concentrated along that finite edge and not being spread out, like it is at the interface's center.

If one wished to address these high SCFs, both types of edges should be filleted (smoothed). As-is, the Kilopower design's ring clamps are closest to failure at these edges.

The heat pipes experience the same stress behavior at the relative locations of those ring clamp edges, a result of the model's interconnection (Figure 4.15).

4.4.2. NOC Postprocessed Maximum Values. Across the heat pipe and ring clamp, the maximum stresses were measured using MOOSE's Postprocessors module. Since maximum allowable stress is a scalar fraction of yield strength (YS) or fracture strength (FS) based on an arbitrary factor of safety, the maximum stresses found will be weighed against the YS or FS (whichever is lower) [11]. This is the fraction to dictate the

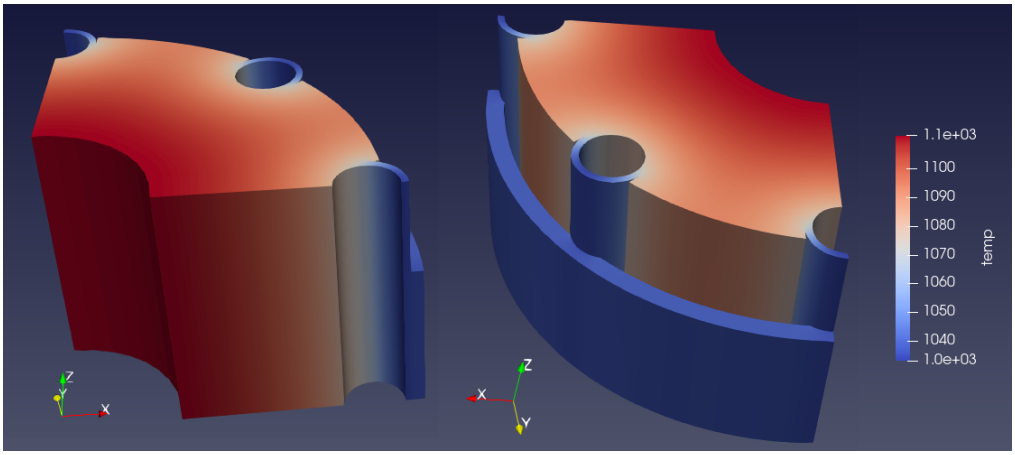

Figure 4.11. Kilopower RCD section with Haynes 230 cladding temperatures (K) during NOC.

candidates' relative performance during NOC using Equation 2.1. It will be referred to as the 'NOC [component] hoop stress fraction' henceforth. Also, temperature and proximity to its limits were found for the cladding candidates, reported as a 'NOC [component] temperature fraction.'

Component temperatures were relatively unchanged among the four claddings, the exception being with SiC-SiC, which displayed lower temperatures for the Fuel and Heat Pipes, but higher for the Ring Clamp, resulting in an overall more even heatmap (Figure 4.16). The differences were only between 5-10 Kelvin, resulting in only a minute difference in NOC Fuel temperature fraction among the four, staying at 0.8 (Figure 4.18). This relatively close melting point for the fuel, unassuaged by cladding choice, may prove a liability during LOCA runs.

However, each candidate's melting / sublimation points led to very different results for NOC Heat Pipe and Ring Clamp temperature fractions. SiC-SiC shined here with its 0.4 fraction from a 2700 K limit, while interestingly enough, Haynes 230, the default material, performed the worst, topping out near 0.7 from a much lower melting point. With all measurements below 1.0, it was safe to say the materials will be fine during Kilopower's

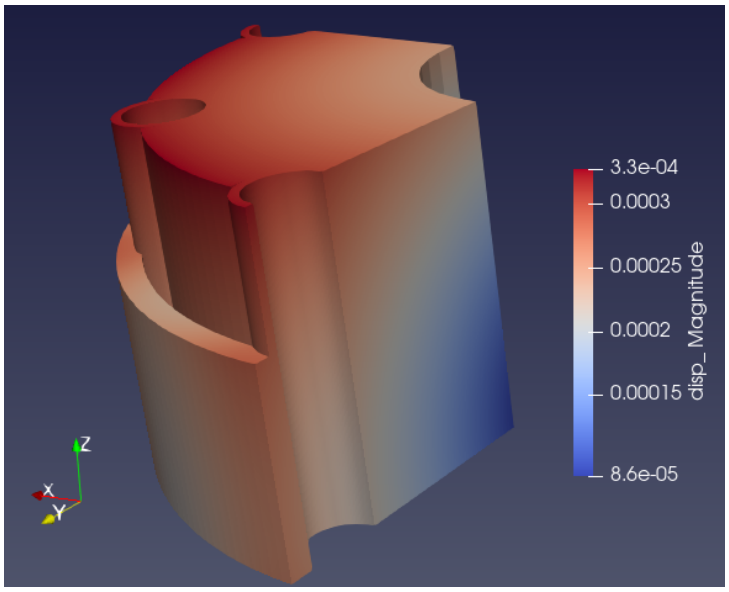

Figure 4.12. Kilopower RCD section with Haynes 230 cladding displacement magnitudes (m) during NOC.

operational parameter of a 1073 K average core and heat pipe temperature. Resistance to failure during a temperature increase will have to be further examined during the LOCA runs.

Maximal hoop stress varies wildly by candidate (Figure 4.17). Haynes 230 displays the lowest, almost matched by FeCrAl, while Zircaloy-4 nearly triples this and is only surpassed by SiC-SiC. Because the YS / FS limit depends closely upon temperatures for three of the four candidates - seen in Figure 2.1 - the high temperatures of this reactor environment very harshly affected the NOC Heat Pipe and Ring Clamp stress fractions for FeCrAl and to a lesser extent Zircaloy-4. The sizeable difference between FeCrAl's component stress fractions is from a temperature-induced difference in limits, changing from 50 MPa for the HP to 30 MPa for the RC. SiC-SiC is a more unique case, for while it has a similar limit to Haynes 230, its own resistance to thermal creep is likely what produced extremely high stresses and rose its fraction so dramatically.

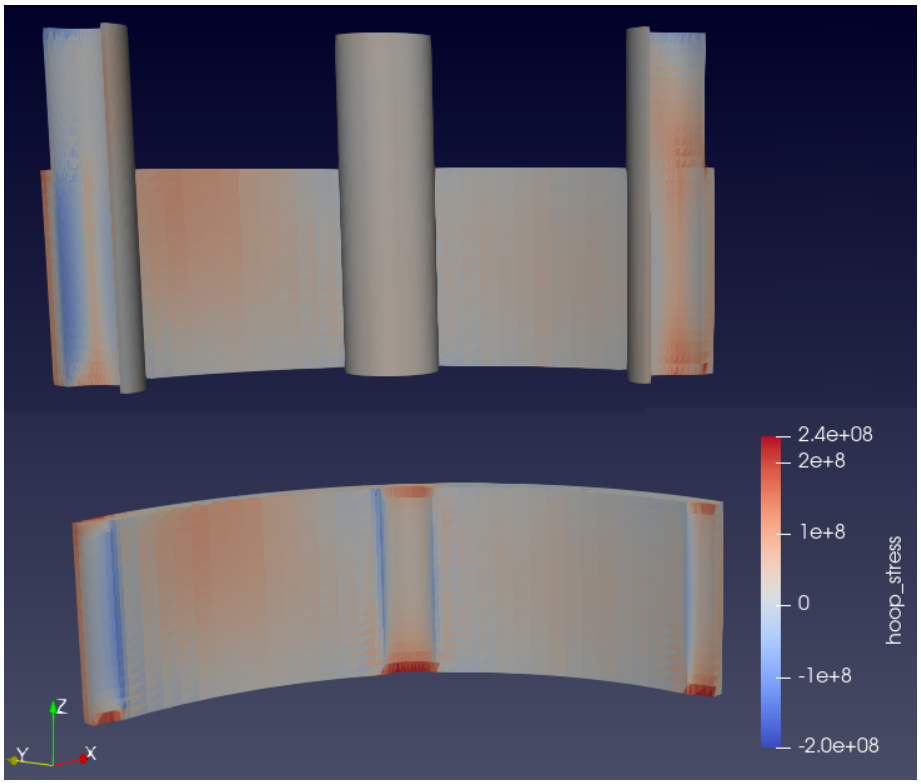

Figure 4.13. Kilopower RCD section with Haynes 230 cladding hoop stress (Pa) during NOC, specifically the ring clamp and heat pipes.

Of all the candidates, Haynes 230 seems most well-equipped for this environment. Its limits are still relatively generous during these operational temperatures and its fractions are all lower than 1.0, meaning its maximum hoop stress and temperatures are less than their limits and theoretically will not have issues during NOC (Figure 4.19).

4.5. LOCA RESULTS AND DISCUSSION

With the *.exd* model, a LOCA was simulated with relative ease. The resulting .exd file of a NOC run that has converged could be loaded into this LOCA script to continue the run. The BC of any heat pipe of choice would be disabled from the latest timestep onward. This way, a temperature / displacement map would be available to start with, much more accurate than any initial conditions defined in the script.

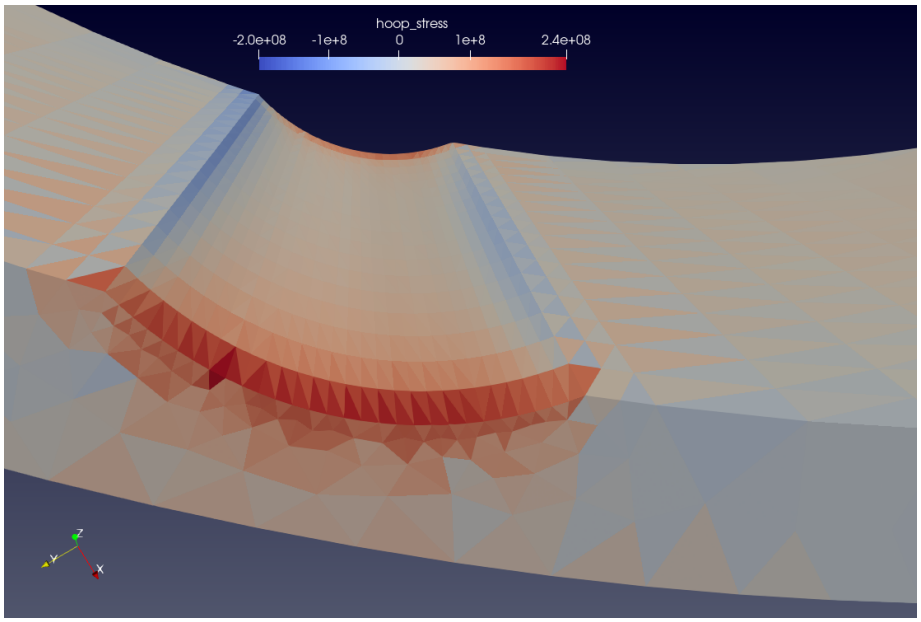

Figure 4.14. Kilopower RCD section with Haynes 230 cladding hoop stress (Pa) during NOC, specifically the ring clamp interface between itself and HP2.

According to the Kilopower team, full power can still be delivered even if several heat pipes (or Stirling engines) fail. Only through the failure of at least three adjacent heat pipes would power level need to be reduced to avoid exceeding the fuel temperature limit [2]. This project will be able to test that proposition for a LOCA in one heat pipe.

4.5.1. LOCA Exodus Output Model. The temperature behavior of all three LOCAs in Figures 4.20, 4.21, and 4.22 is at a surface level to be expected - temperature is higher at the site of the LOCA and thus causes overall increase in temperature, until a steady state temperature level is reached with the new levels of convective heat flux. It does not result in unchecked heat generation.

However, the results for an HP2 LOCA (Figure 4.21) are much higher than HP1 and HP3, which are identical, but mirrored, as should be anticipated. This is likely due to the nature of the assumptions being made. With symmetrical BCs at both angular ends, the behavior at HP1 or HP3 is being reflected across. Essentially, this model represents a

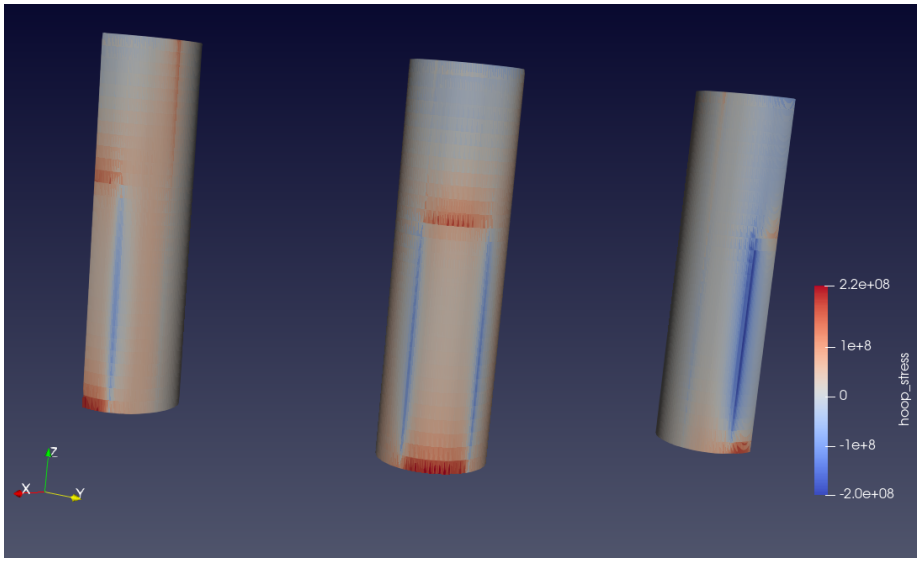

Figure 4.15. Kilopower RCD section with Haynes 230 cladding hoop stress (Pa) during NOC, specifically the three heat pipes, viewed at the direction of their interfaces with the ring clamp.

LOCA in two heat pipes at direct opposite ends of the core. Those reflections mean that an HP2 LOCA actually represents a LOCA in *four* heat pipes. One would need to model another quarter of the reactor to represent a LOCA in only one heat pipe.

Displacement behavior in an HP1 LOCA (Figure 4.23) is nearly identical to NOC behavior (Figure 4.12), showing similar near-uniform expansion in the positive axes. The exception being the areas of higher temperature, which have a slightly higher displacement magnitude.

The hoop stresses during an HP1 LOCA (Figure 4.24) also reflect very similarly to that of NOC (Figure 4.13), with one exception: the interface between HP1 and the ring clamp has much lower SCFs, likely due to the higher temperatures causing higher thermal expansion in the clamp relative to the other heat pipe interfaces. That burden of stress was effectively transferred to the opposite side of the ring clamp, where this sector experiences much higher stress than the other heat pipes' sectors. Since the nearby BC does not allow

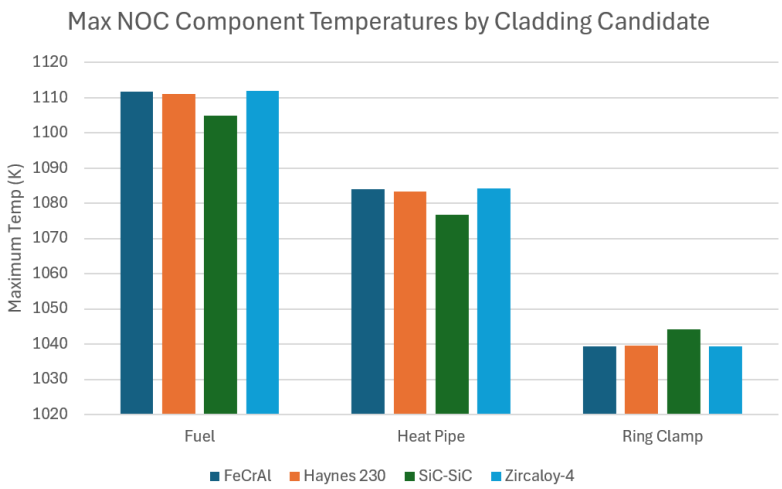

Figure 4.16. Maximum temperatures of the NOC runs, sorted by component and candidate cladding.

for angular movement, only radial and axial, this sector is likely experiencing more pressure to bend inward, thus increasing the local outside hoop stress. This interface behavior is mirrored during an HP3 LOCA in Figure 4.25, and is thus unlikely to be an anomaly.

To save further computational costs from a larger mesh and to keep the failure scenario more reasonable, the LOCA scenario with HP1 failing was chosen for the main analysis going forward. This will simply be referred to as an HP1 LOCA, but will be properly noted where necessary that it represents two heat pipes failing.

4.5.2. LOCA Postprocessed Maximum Values. Like with NOC, the postprocessed output looked for maximum hoop stress across all elements of the ring clamp and heat pipes, with its own accompanying 'LOCA [component] hoop stress fraction'. Also, temperature and proximity to its limits were found for the cladding candidates, reported as a 'LOCA [component] temperature fraction' (Equation 2.1).

As a LOCA is a time-dependent incident, where temperatures and stresses begin to increase after the accident occurs, these comparative measures tracked the maximums along each timestep.

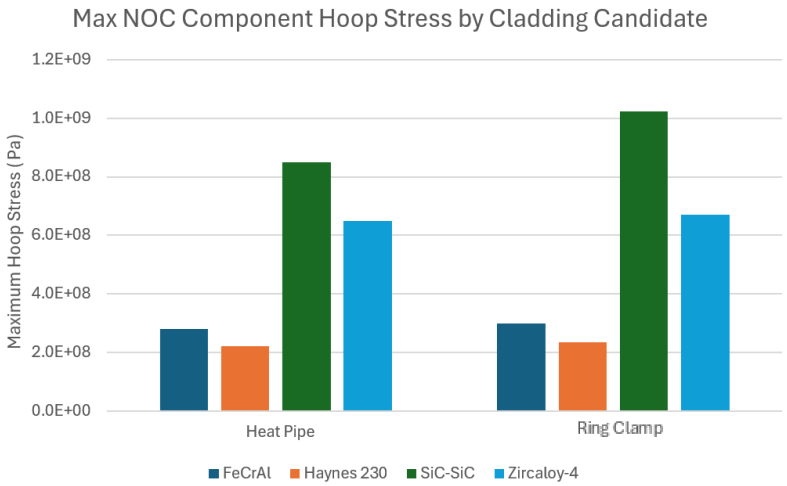

Figure 4.17. Maximum hoop stresses of the NOC runs, sorted by component and candidate cladding.

The overall beginning and end behavior of the LOCA temperatures (Figure 4.26) match their NOC equivalents (Figure 4.16). SiC-SiC displays lower, more heat-resistant temperatures, with most of the rest staying close together. In terms of LOCA temperature fractions, in Figure 4.28, there is relatively little change with a LOCA in two heat pipes and no unusual behaviors.

As the Kilopower team claimed, no component temperature limits were breached in this LOCA scenario of less than three heat pipes. This ability for the working heat pipes to, in a sense, pick up the others' slack (alongside the relatively small distances between each pipe) prevented any drastically high local maximums that would have resulted in failure. This speaks to how well-designed the Kilopower system is. So, once again, SiC-SiC performs the best with a 0.425 LOCA Ring Clamp and Heat Pipe temperature end fraction and Haynes 230 performs the worst with a 0.75 end fraction. The LOCA Fuel temperature end fraction is still less than even 0.85 across all of the candidates; still relatively close to unity, but a manageable change.

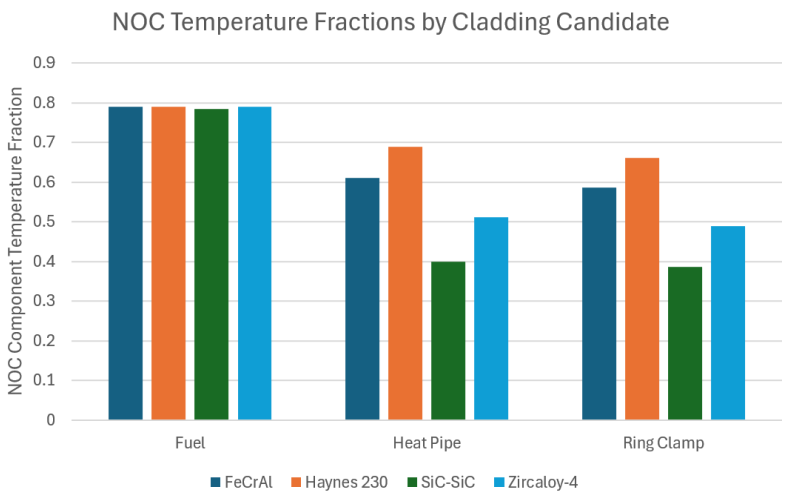

Figure 4.18. Temperature fractions of the NOC runs, sorted by component and candidate cladding.

The raw hoop stresses measured during LOCA (Figure 4.27) did not exhibit any unusual behavior compared to NOC performance in Figure 4.17. All the values found at the start were merely proportionally exemplified by the endpoint. However, factoring in their limits with LOCA hoop stress fractions in Figure 4.29 led to some radical effects on FeCrAl and especially Zircaloy-4 due to the slight change in temperature. This is more evidence to suggest that these materials simply are not meant to operate at the high temperatures of Kilopower. SiC-SiC, with its relatively unchanging flexural strength, matches Haynes 230 for endurance against LOCA conditions. Yet even Haynes 230's LOCA stress fraction exceeds unity after a two heat pipe LOCA, suggesting that even though it would be able to operate thermally, the ring clamps and heat pipes would be at danger of fracture.

Thus, all four claddings do not survive a two-heat pipe LOCA. However, as mentioned before, due to a lack of hoop stress benchmarking of the Kilopower reactor, this project ultimately only needs the comparative data of the four claddings. Each individ-

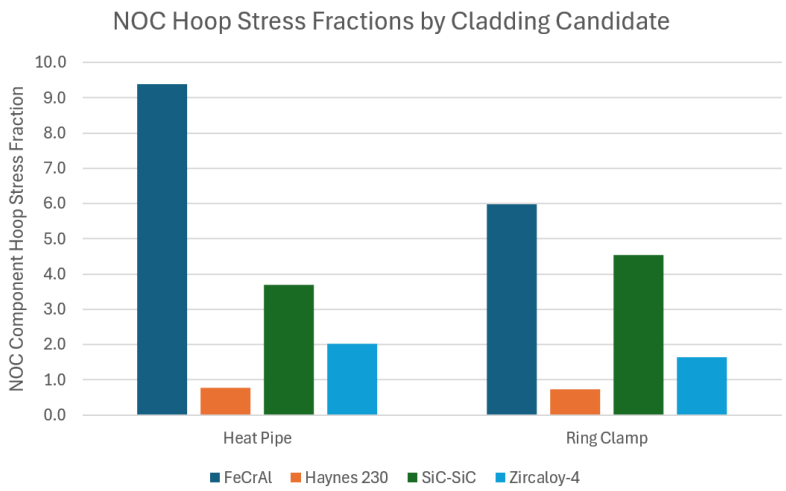

Figure 4.19. Hoop stress fractions of the NOC runs, sorted by component and candidate cladding.

ual run does not have to be accurate to the Kilopower reactor, so long as the conditions of *any* such high-temperature microreactor are being well-simulated and the candidates' performances are accurate in comparison to each other.

Haynes 230 performs the closest to within limits during a one-heat pipe LOCA, making it still the best choice for such a reactor in terms of accident-prevention.

4.6. MOOSE-MCNP ITERATION

With axial temperature profiles for the MOOSE model, it was now possible to transfer that data into the MCNP model and perform axial power profile calculations again, to see if the updated temperatures had a significant effect on the neutronics. Conservation of mass will be applied, so the MCNP model will not change size to account for thermal expansion and thus will not change density. The core was split into 28 sections, assigned the average temperature from each MOOSE model's section.

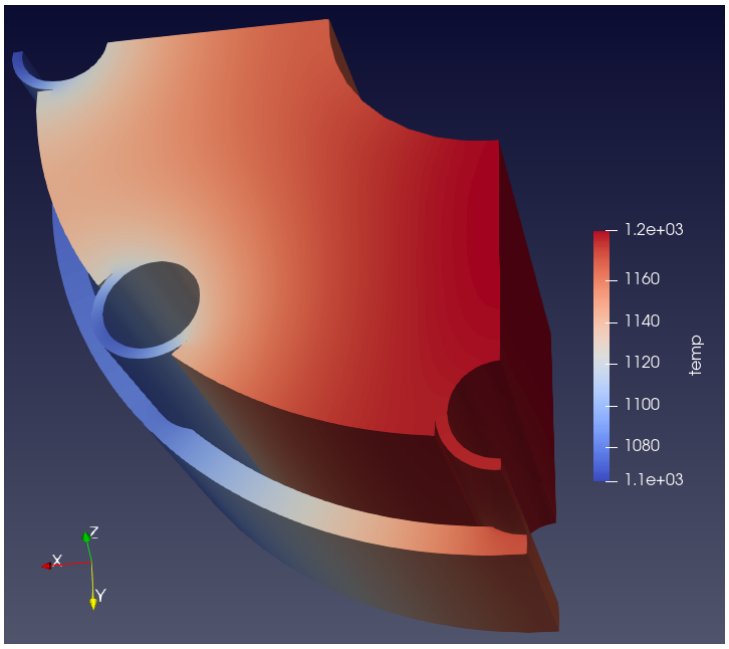

Figure 4.20. Kilopower RCD section with Haynes 230 cladding temperatures (K) during a LOCA in HP1.

The axial temperature differences were minute enough to result in only a 0.6% difference in fission rate, at most (Figures 4.30 and 4.31). This was not deemed large enough to be accounted for in future model runs.

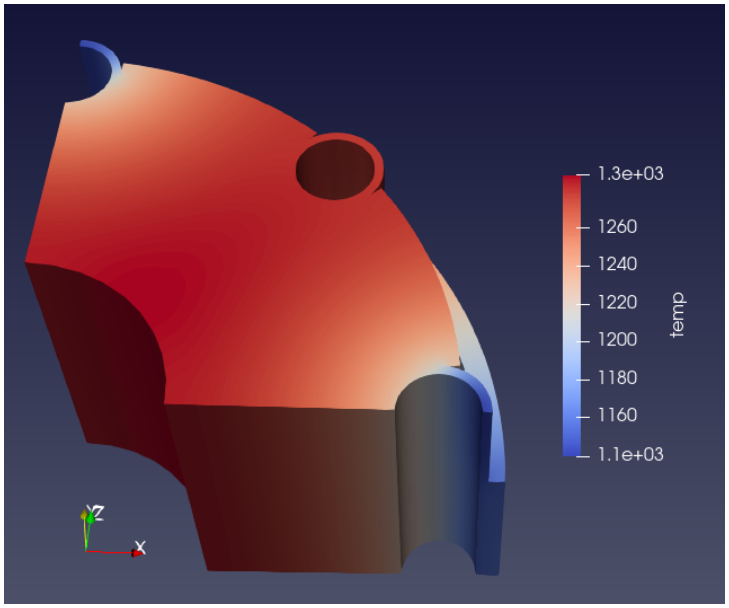

Figure 4.21. Kilopower RCD section with Haynes 230 cladding temperatures (K) during a LOCA in HP2.

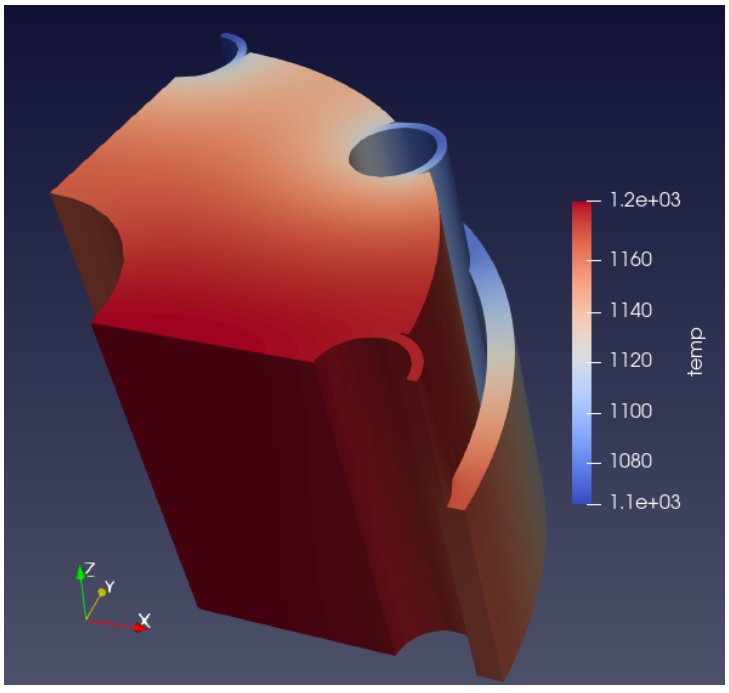

Figure 4.22. Kilopower RCD section with Haynes 230 cladding temperatures (K) during a LOCA in HP3. Note the near-identical heatmap to Figure 4.20

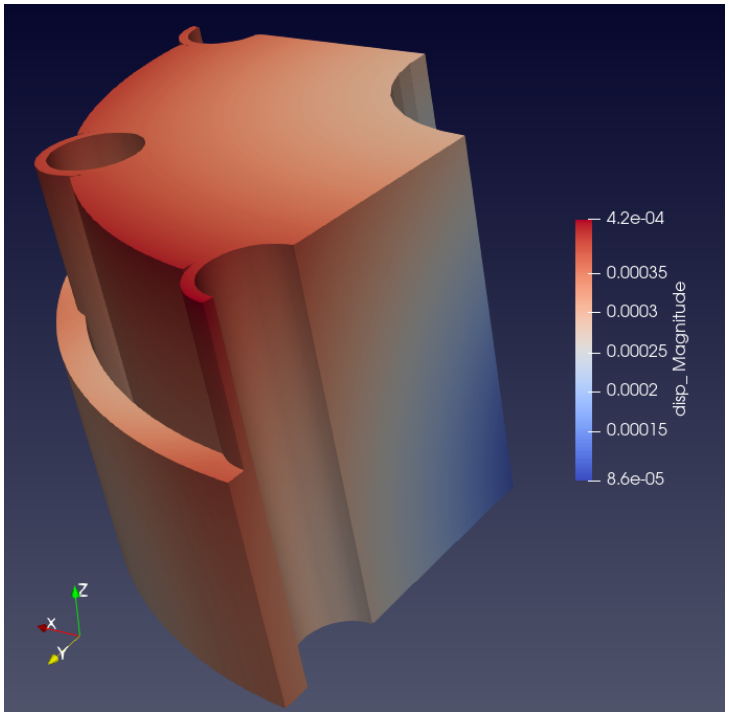

Figure 4.23. Kilopower RCD section with Haynes 230 cladding displacement magnitudes (m) during a LOCA in HP1.

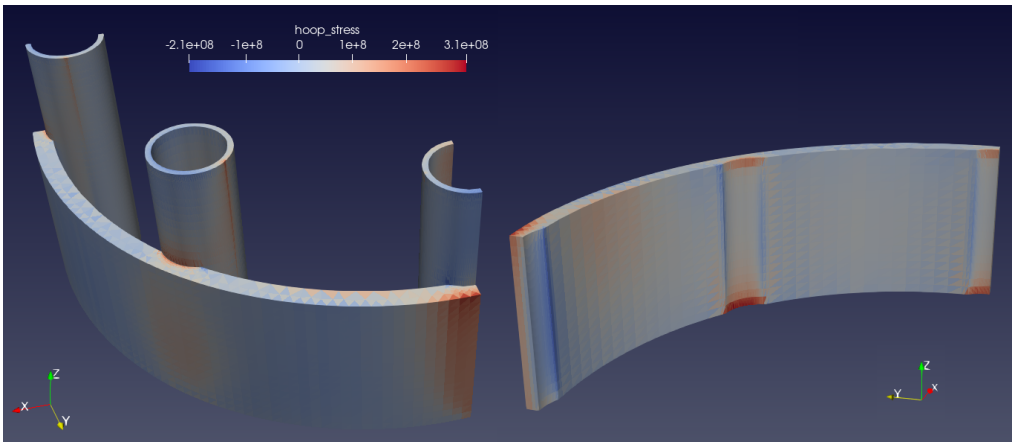

Figure 4.24. Kilopower RCD section with Haynes 230 cladding hoop stresses (Pa) during a LOCA in HP1, specifically the ring clamp and heat pipes.

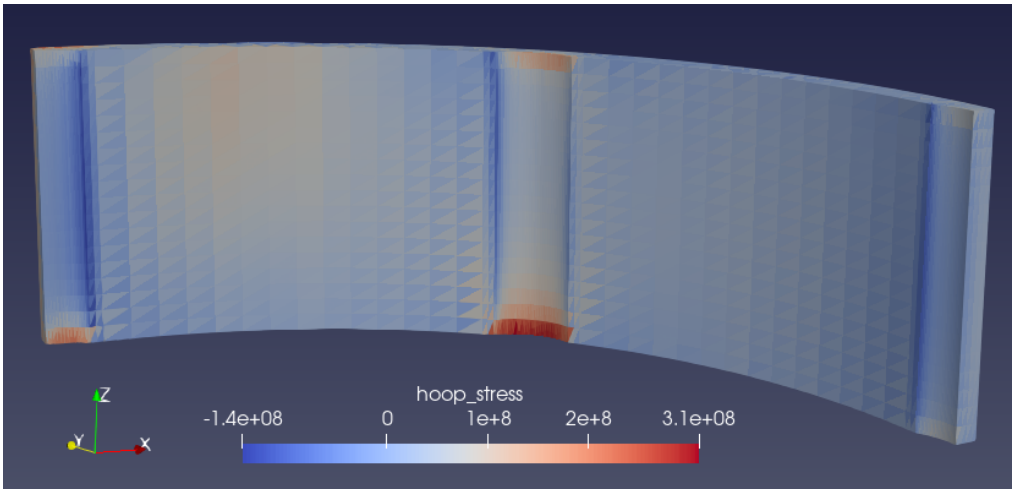

Figure 4.25. Kilopower RCD section with Haynes 230 cladding hoop stresses (Pa) during a LOCA in HP3, specifically the ring clamp. Note the similarity in behavior at the HP3 interface to the HP1 interface in Figure 4.24.

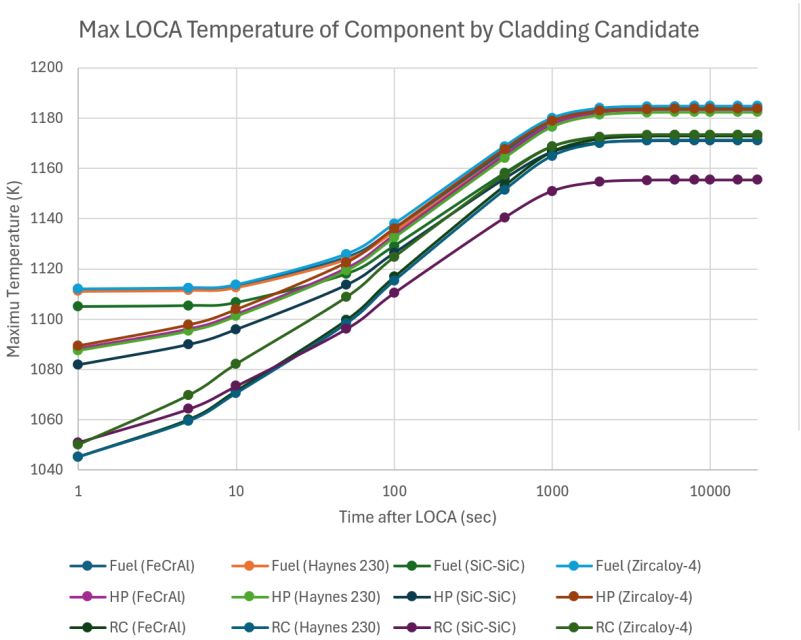

Figure 4.26. Maximum temperatures of the LOCA runs, sorted by component and candidate cladding. HP is heat pipe and RC is ring clamp.

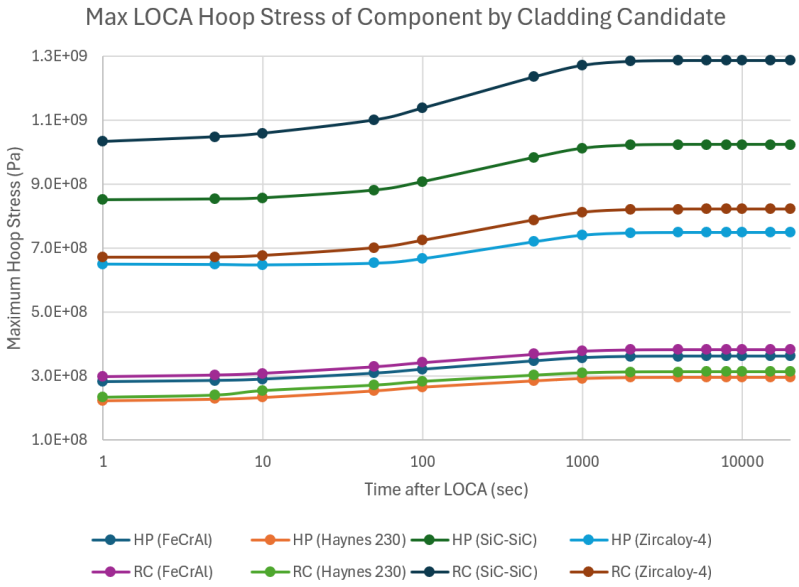

Figure 4.27. Maximum hoop stresses of the LOCA runs, sorted by component and candidate cladding. HP is heat pipe and RC is ring clamp.

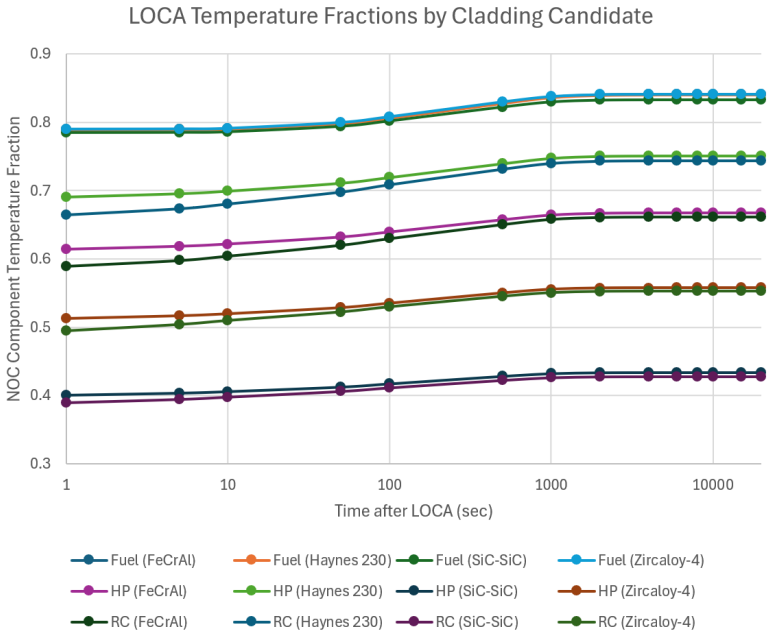

Figure 4.28. Temperature fractions of the LOCA runs, sorted by component and candidate cladding. HP is heat pipe and RC is ring clamp. Fuel (Zircaloy-4), Fuel (Haynes 230), and Fuel (FeCrAl) occupy nearly the same values.

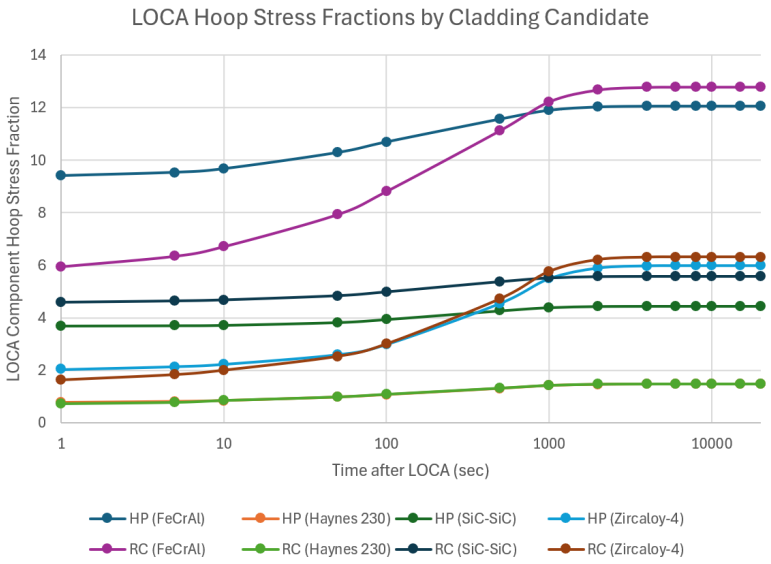

Figure 4.29. Hoop stress fractions of the LOCA runs, sorted by component and candidate cladding. HP is heat pipe and RC is ring clamp. HP (Haynes 230) and RC (Haynes 230) occupy nearly the same values.

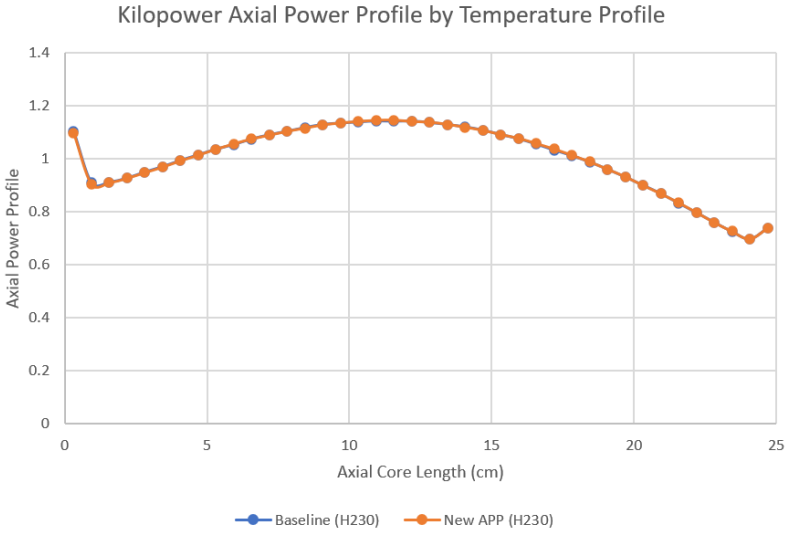

Figure 4.30. Axial power peaking of the Kilopower fuel block, comparing a uniform axial temperature profile and one imported from MOOSE.

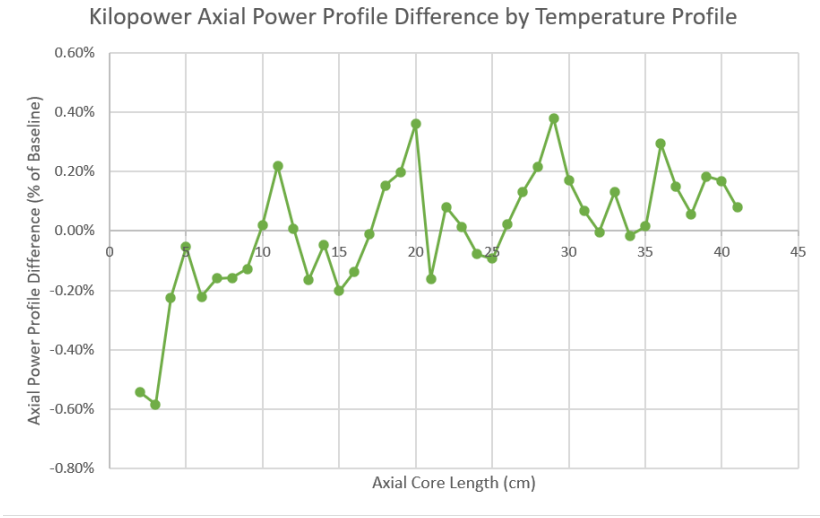

Figure 4.31. Percent difference in axial power peaking of the Kilopower fuel block, comparing a uniform axial temperature profile and one imported from MOOSE.

5. UQ / SA

5.1. PRELIMINARY STEPS

5.1.1. Methodology. A PCE begins with the assignment of uncertainty to input variables. When uncertainties are introduced, the model becomes non-deterministic:

$$M(u, a) = 0 \tag{5.1}$$

If M represents the model, u is the model output response and $a = \{a_1, a_2, ..., a_n\}$ is the set of inputs. If these input parameters a are uncertain, they can be represented with a set of independent random variables $\xi = \{\xi_1, \xi_2, ..., \xi_n\}$, which would also make the output response u stochastic, so $u(\xi)$.

The goal of the PCE is to measure the statistical moments and probability density function (PDF) of $u(\xi)$. In this case, the most important moments will be mean and standard deviation. These are calculated with:

$$< u >= \int u f_u(u) du \tag{5.2}$$

$$\sigma_u^2 = \int (u - < u >)^2 f_u(u) du \tag{5.3}$$

$f_u(u)$ is the PDF of u. These integrals are computed numerically. Since this PCE is non-intrusive, this will not involve modification of the MCNP or MOOSE scripts, as it will be treated as a black box.

This step began with a parametric SA on each of the six material properties to see which affected the results the most. This involved running the same code twelve times, twice for each property, with either a 5% increase or decrease. The resulting maximum stress would be plotted against the baseline maximum stress to see which property changes had the largest impact. This informed which would be a part of the PCE.

The advantage of non-intrusive PCE is that it allows for non-linear behavior to be captured. Any properties that exhibit this would be invaluable to the PCE. A deterministic model would require much more effort and computational cost to capture the complex polynomials that represent interactions between the changes in inputs.

The SA was done for both LOCA and NOC, the same parameters as the previous runs: 20,000 second transient runs until a steady-state was found, with the LOCA runs using the NOC *.exd* mesh output as initial conditions. Only Haynes 230 underwent a SA, as even if an SA for the other candidates showed radically different results, to keep the analysis consistent only one set of input variables would be chosen to receive PDFs in the PCE. These runs looked at maximum fuel temperature, ring clamp temperature, and ring clamp hoop stress.

5.1.2. Results. Thermal conductivity clearly was the only property with a noticeable effect on fuel or ring clamp max temperatures in either conditions (Figures 5.1, 5.2, 5.4, and 5.5). The effect itself is also relatively small, of only 0.1-0.8 K compared to temperatures in the 1000's. This was deemed not significant enough to investigate further.

Thermal expansion coefficient had the most impact on hoop stress for both the LOCA and NOC runs (Figures 5.3 and 5.6). This was expected, as it is a property that directly relates to material displacement, the core of the stress calculations. However, Young's Modulus (YM) and Poisson's Ratio (PR) also had a noticeable impact, including some non-linear behavior of the former during LOCA runs, where both its increase and decrease resulted in an increase of maximum hoop stress. It was decided that these two properties, instead of thermal expansion coefficient, would be part of the PCE. This was because (in the

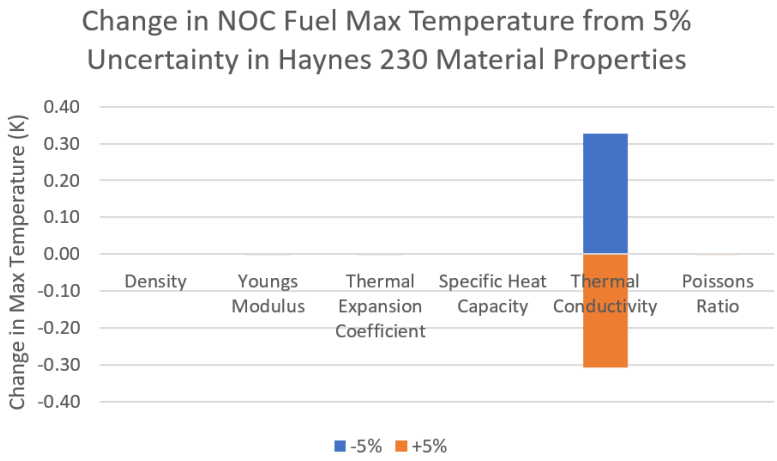

Figure 5.1. Differences in the maximum fuel temperature from the final MOOSE NOC runs when a 5% change is applied to each material property of the cladding.

NOC scenario at least), PR and YM caused roughly equal magnitudes of sensitivity. Pairing a particularly sensitive variable with another less sensitive one may cause the effects of the latter to be overshadowed, hence why thermal expansion coefficient was not chosen. And the non-linear behavior of YM is precisely what PCE is best utilized to capture, making this a good showcase of its capabilities.

5.2. POLYNOMIAL CHAOS EXPANSION

5.2.1. Methodology. With variables chosen, the PCE can begin. The input variables are given PDFs and a surrogate model can be created:

$$u(x;\xi) = \sum_{i=0}^{N} u_i(x)\psi_i(\xi) \tag{5.4}$$

A model with n uncertain inputs has a stochastic output $u(x;\xi)$ that can be represented by Equation 5.4, where u_i are the deterministic polynomial coefficients and ψ_i are the multi-dimensional orthogonal polynomial functions of independent random variables $\xi =$

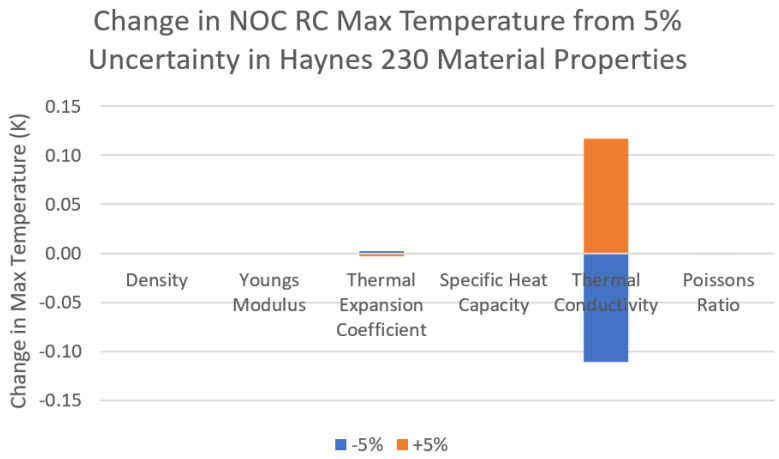

Figure 5.2. Differences in the maximum ring clamp temperature from the final MOOSE NOC runs when a 5% change is applied to each material property of the cladding.

$\{\xi_1, \xi_2, ..., \xi_n\}$. The PDF of ξ is given by:

$$\mathbf{W}(\xi) = \prod_{i=1}^{n} W_i(\xi_i) \tag{5.5}$$

The distribution of ξ is simply the joint probabilities of all individual ξ_i's, represented by $W_i(\xi_i)$.

The sum of polynomial terms $N + 1$ in Equation 5.4 is in relation to the maximum order of the polynomial p being expanded and the number of uncertain inputs n as follows:

$$N + 1 = \frac{(n + p)!}{n!p!} \tag{5.6}$$

Because of the Kronecker delta $\sigma_i j$, polynomials ψ_i are orthogonal as such:

$$< \psi_i \psi_j > = < \psi_i^2 > \sigma_{ij} \tag{5.7}$$

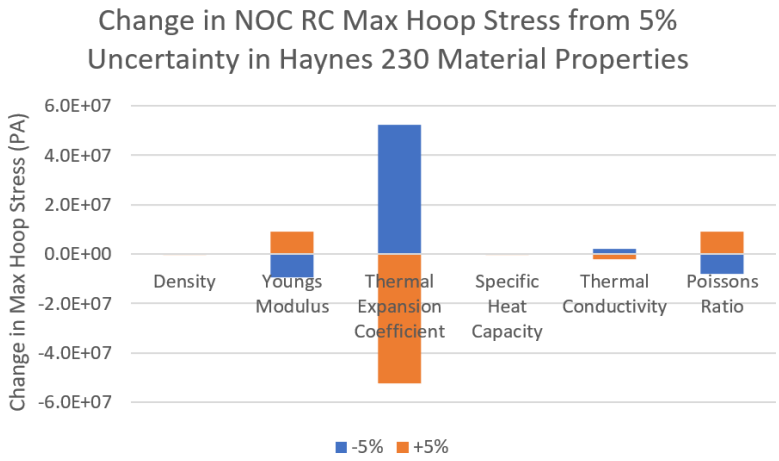

Figure 5.3. Differences in the maximum ring clamp hoop stress from the final MOOSE NOC runs when a 5% change is applied to each material property of the cladding.

$< \psi_i \psi_j >$ is also defined as:

$$< \psi_i \psi_j > = \int_{\xi} \psi_i(\xi) \psi_j(\xi) \mathbf{W}_{\xi} d(\xi) \tag{5.8}$$

Output u's mean is found via:

$$< u > = \int_{\xi} \mathbf{W}_{\xi} d(\xi) = u_0 \tag{5.9}$$

Due to orthogonality, PC coefficient u_0 is the mean of $u(x;\xi)$, the output response. The response's variance is computed by:

$$\begin{aligned} \sigma_u^2 &= < (u - < u >)^2 > \\ &= \int_{\xi} \left\{ \sum_{i=1}^{N} u_i(x) \psi_i(\xi) \right\}^2 \mathbf{W}_{\xi} d(\xi) \\ &= \sum_{i=1}^{N} u_i^2(x) < \psi_i^2 > \end{aligned} \tag{5.10}$$

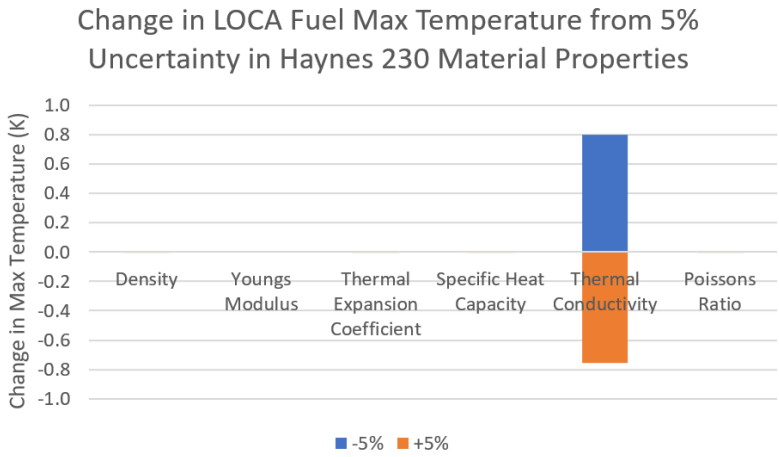

Figure 5.4. Differences in the maximum fuel temperature from the final MOOSE LOCA runs when a 5% change is applied to each material property of the cladding.

To perform UQ on output responses for inputs with any individually-given probability, the polynomials must be generalized such that:

$$\begin{aligned} u(x;\xi^1) &= u_0 + u_1(x)\psi_1(\xi^1) + u_2(x)\psi_2(\xi^1) + \ldots + u_N(x)\psi_N(\xi^1) \\ u(x;\xi^2) &= u_0 + u_1(x)\psi_1(\xi^2) + u_2(x)\psi_2(\xi^2) + \ldots + u_N(x)\psi_N(\xi^2) \\ &\ldots \\ u(x;\xi^M) &= u_0 + u_1(x)\psi_1(\xi^M) + u_2(x)\psi_2(\xi^M) + \ldots + u_N(x)\psi_N(\xi^M) \end{aligned} \tag{5.11}$$

can represent them as a system of equations using Equation 5.4 as its base, M being the total number of samples generated for ξ (ξ^1, ξ^1, ... , ξ^1). a_i and u_i are the corresponding input parameter and model response for each ξ_i. It can be rewritten in matrix form as:

$$\begin{pmatrix} \psi_0(\xi^1) & \psi_1(\xi^1) & \psi_2(\xi^1) & \ldots & \psi_P(\xi^1) \\ \psi_0(\xi^2) & \psi_1(\xi^2) & \psi_2(\xi^2) & \ldots & \psi_P(\xi^2) \\ \ldots & \ldots & \ldots & & \ldots \\ \psi_0(\xi^M) & \psi_1(\xi^M) & \psi_2(\xi^M) & \ldots & \psi_P(\xi^M) \end{pmatrix} \times \begin{pmatrix} u_0 \\ u_1 \\ \ldots \\ u_P \end{pmatrix} = \begin{pmatrix} u(\xi^1) \\ u(\xi^2) \\ \ldots \\ u(\xi^M) \end{pmatrix} \tag{5.12}$$

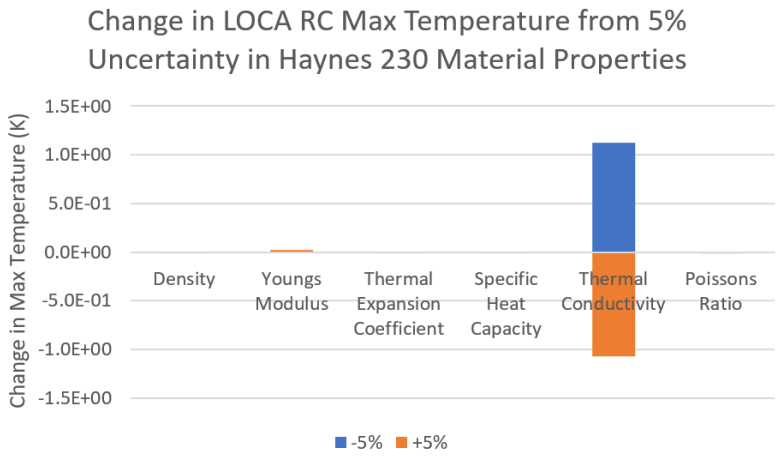

Figure 5.5. Differences in the maximum ring clamp temperature from the final MOOSE LOCA runs when a 5% change is applied to each material property of the cladding.

or

$$DU = B \tag{5.13}$$

Should the sum M of equations be higher than sum P of unknowns, the solution of Equation 5.12 can be found using least squares regression as such:

$$U = (D^T D)^{-1} D^T B \tag{5.14}$$

This is the Wiener-Askey scheme using Legendre polynomials, which are most efficient for uniformly distributed random variables and as such are befitting of this study [44]. The system of equations (Equation 5.11) is solved using regression and its statistical moments (mean, standard deviation, etc.) are found as the final part of this step.

Practically, in a PCE, certain M&S input variables are assigned distributions. Those are repeatedly sampled, creating a deck of many similar input codes, with the only difference being the values for those variables. Those codes are ran and their results collated. If the results are sensitive to the uncertainty in the variables, then they will themselves form a distribution [45].

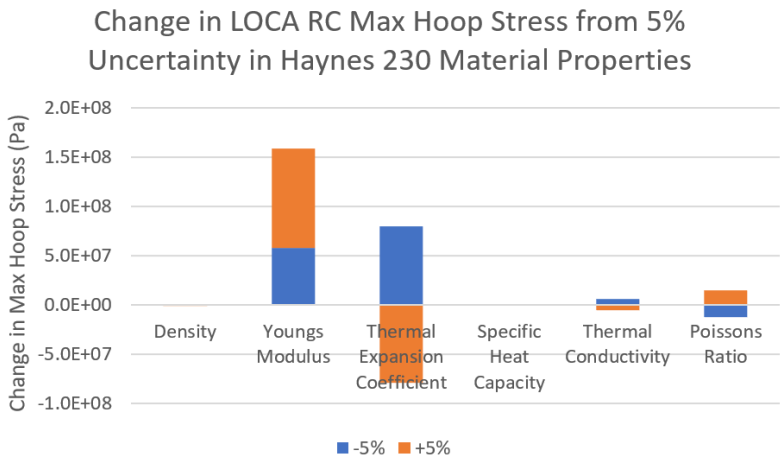

Figure 5.6. Differences in the maximum ring clamp hoop stress from the final MOOSE LOCA runs when a 5% change is applied to each material property of the cladding.

The PCE performed in this project was to find the distributions of stress fractions during NOC and stress fractions and temperature fractions during a LOCA. Then, compare those distributions with the respective limits and with each other, finding which candidates' property uncertainties would have a higher likelihood of exceeding limits and thus would need to be prioritized for further experimental research.

The creation of the input decks for PCE was performed using Python, specifically the package *chaospy* for its ability to generate and sample distributions. A template for the MOOSE input was written to and copied with each sample from their respective distribution. The subsequent *.csv* files generated by the MOOSE runs were collected and sorted using *pandas*, another package.

5.2.2. Results. This project believes Figures 5.7, 5.8, 5.10, and 5.11 show that 50 samples from each configuration were enough to represent their normal distributions and illustrate any divergent behavior in the outputs. Figures 5.9 and 5.12 display uniformity among the candidate claddings.

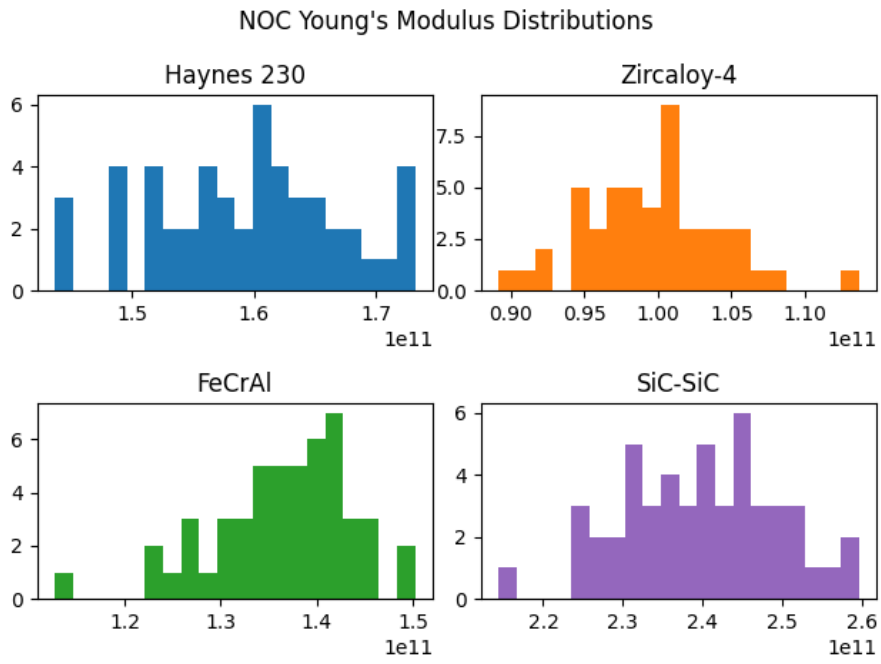

Figure 5.7. Distributions of Young's Modulus among the NOC UQ runs by candidate cladding.

5.3. SOBOL' INDICES

5.3.1. Methodology. With UQ finished, the next step was to perform a more robust SA on the PCE results using Sobol' sensitivity. Like non-intrusive PCE, Sobol' indices allow for a 'black box' approach to the model input / output and don't require modification of the original M&S. The indices are used to determine the influence of individual inputs on the variance of the output, with the sensitivity index S_j, written as:

$$S_j = \frac{V_j}{V} \tag{5.15}$$

The sensitivity of the j^{th} output parameter comes from total variance V and V_j, the variance contribution from the j^{th} input parameters.

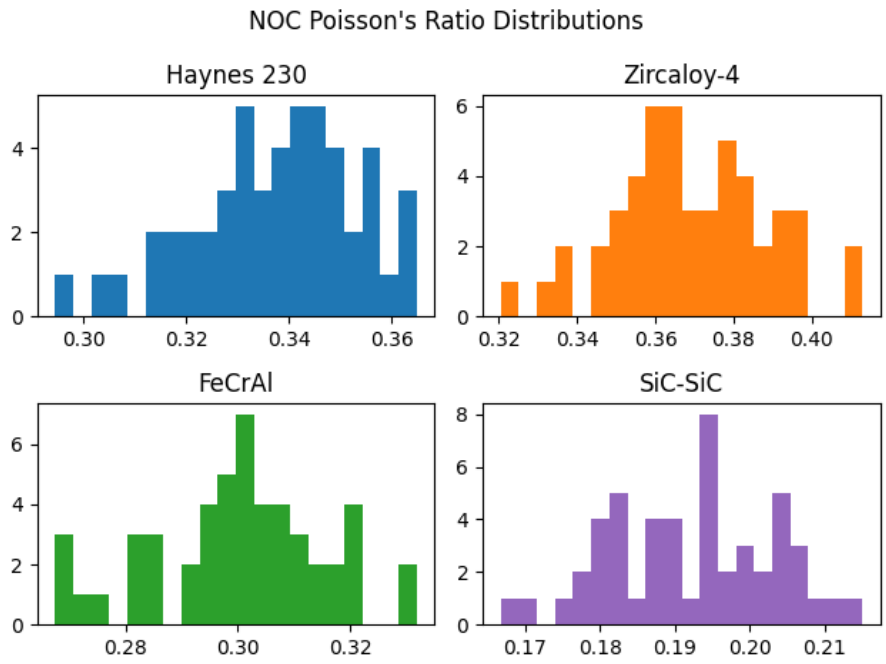

Figure 5.8. Distributions of Poisson's Ratio among the NOC UQ runs by candidate cladding.

Sobol' indices require user-defined distributions for input *and* output to be sampled from. Since the M&S software operates as a black box, its output distributions are undefined. This means code is needed to either define a distribution from the output data or create a surrogate model connecting the input and output samples (which represents the black box). Using *chaospy*, the latter method was chosen. Several polynomial orders were tested, with first-order being, hands-down, the best representation when comparing the 'expected' value from the surrogate model to the MOOSE model's results.

Following the PCE methodology previously outlined, surrogate models of each of the eight runs (four NOC, four LOCA) were created. These models were used for calculations of the Sobol' indices (for the uncertain input parameters), as well as mean and standard deviation (of the output).

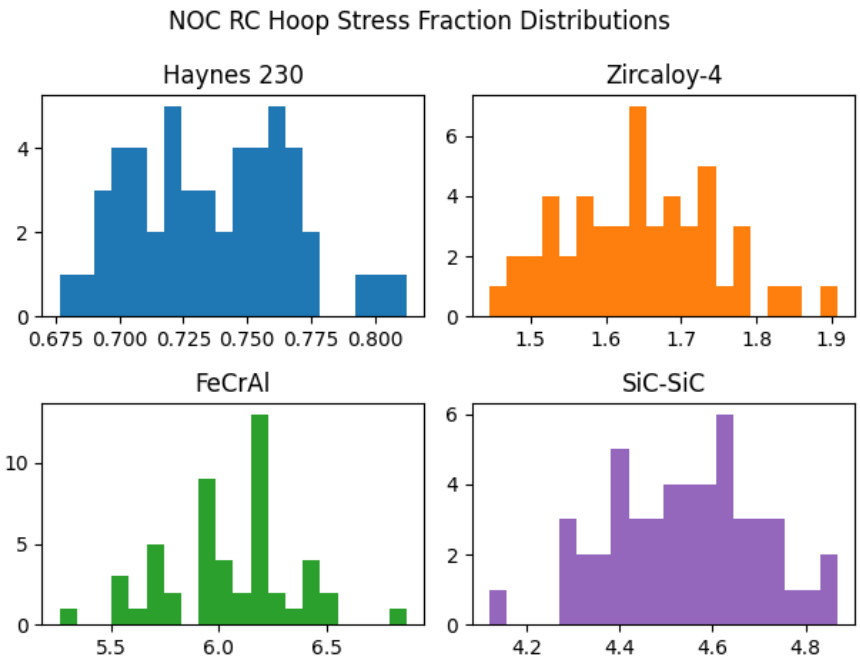

Figure 5.9. Distributions of ring clamp hoop stress fractions among the NOC UQ runs by candidate cladding.

5.3.2. Results. Taking 10,000 samples from each surrogate model gives Figures 5.13 and 5.14. The 'noise' in some of the sampling (for example LOCA - FeCrAl compared to the smoother LOCA - SiC-SiC), is being accounted by the model, as repeated runs capture such behavior from Figures 5.9 and 5.12. This is an example of how *chaospy* extrapolates behavior from the existing input-output data, making these surrogate models that much more robust. And this likely originates in the Sobol' Indices for each cladding (Figure 5.15), where SiC-SiC hoop stress is revealed to be near-wholly dependent on Young's Modulus and not Poisson's Ratio. This one-variable dependency likely creates little cross-variable interaction in the polynomial and results in a more uniform distribution.

The other candidates vary in the impact YM has vs PR. No notable information was gleaned, besides a statement that both have a substantial impact. The non-linear behavior of YM in the preliminary LOCA SA (Figure 5.6) for RC maximum hoop stress was not

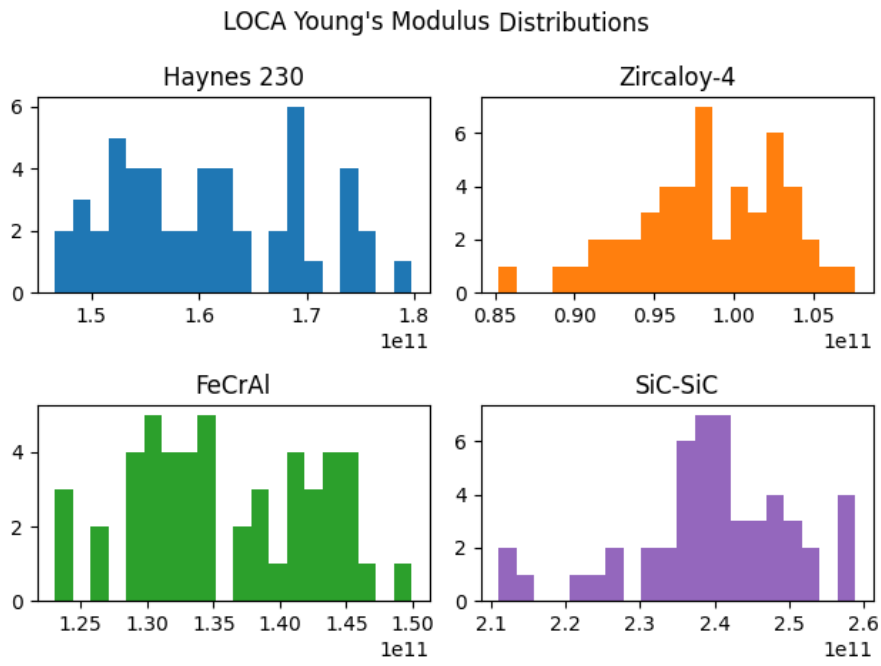

Figure 5.10. Distributions of Young's Modulus among the LOCA UQ runs by candidate cladding.

captured here, implying a convergence error in the those tests that resulted in outliers. Since those specific results had no impact on the path forward, they were not re-done. This further indicates that the relations between input and output are entirely first-order for the MOOSE model.

The tight relationship between the expected stress fractions of the MOOSE and surrogate model runs in Table 5.1 represent the latter's accuracy of the original material. The standard deviation is a measure of the sensitivity each configuration's maximum ring clamp hoop stress fraction. Its raw values are weighted by the expected values, so finding the standard deviation as a percentage was deemed more useful. Haynes 230 and SiC-SiC are relatively close in percent sensitivity, the latter being the lowest. They are followed by Zircaloy-4 and FeCrAl in order.

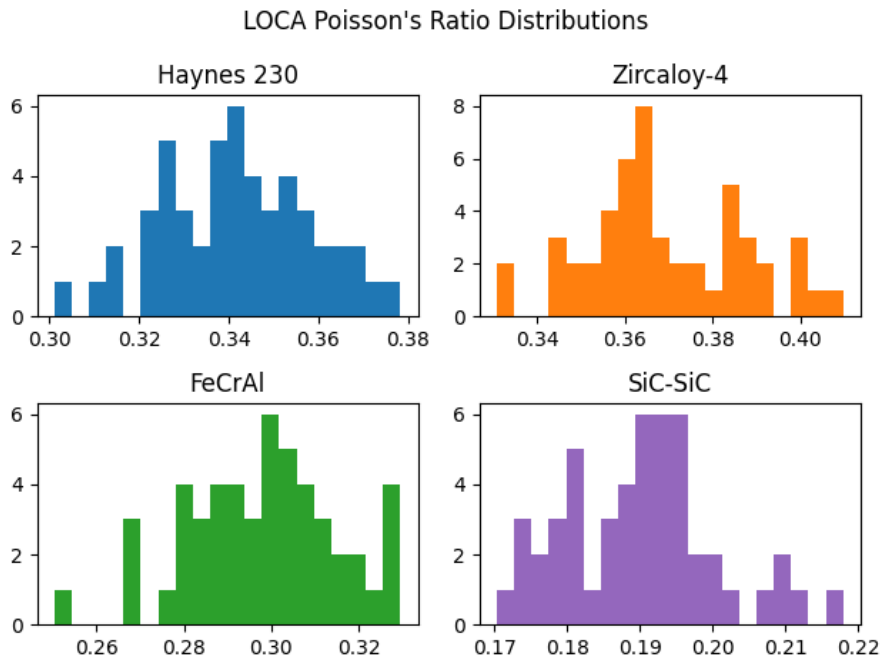

Figure 5.11. Distributions of Poisson's Ratio among the LOCA UQ runs by candidate cladding.

Although the hoop stress fractions for FeCrAl are already *much* higher than unity, meaning that efforts to find more definitive material properties will not move the needle much on their applicability to Kilopower-like reactors, Zircaloy-4 at NOC is close enough to warrant more material property investigations at higher temperatures. Should the hoop stress fraction be ultimately lowered past 1, it may become a viable material for these applications.

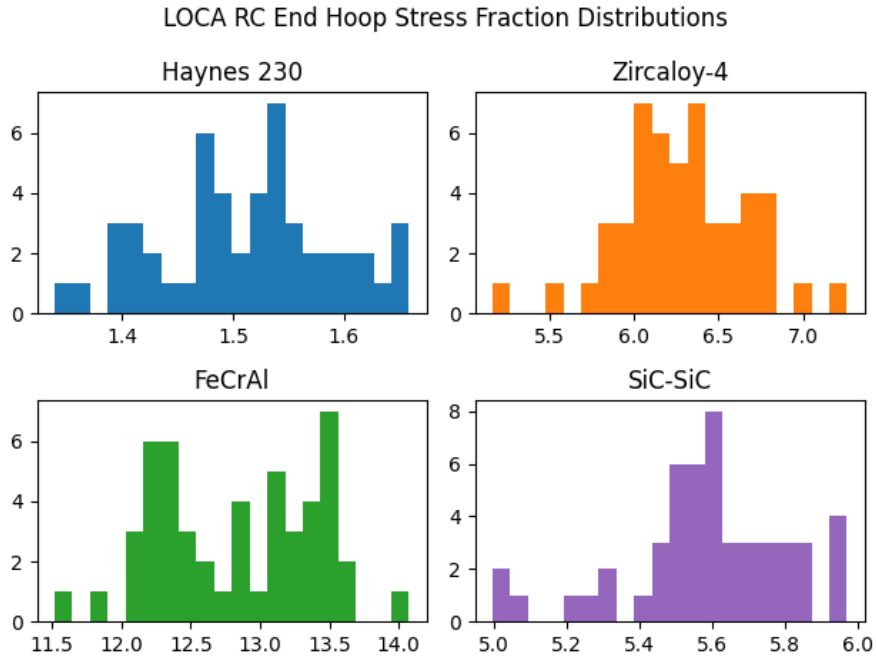

Figure 5.12. Distributions of ring clamp end timestep hoop stress fractions among the LOCA UQ runs by candidate cladding.

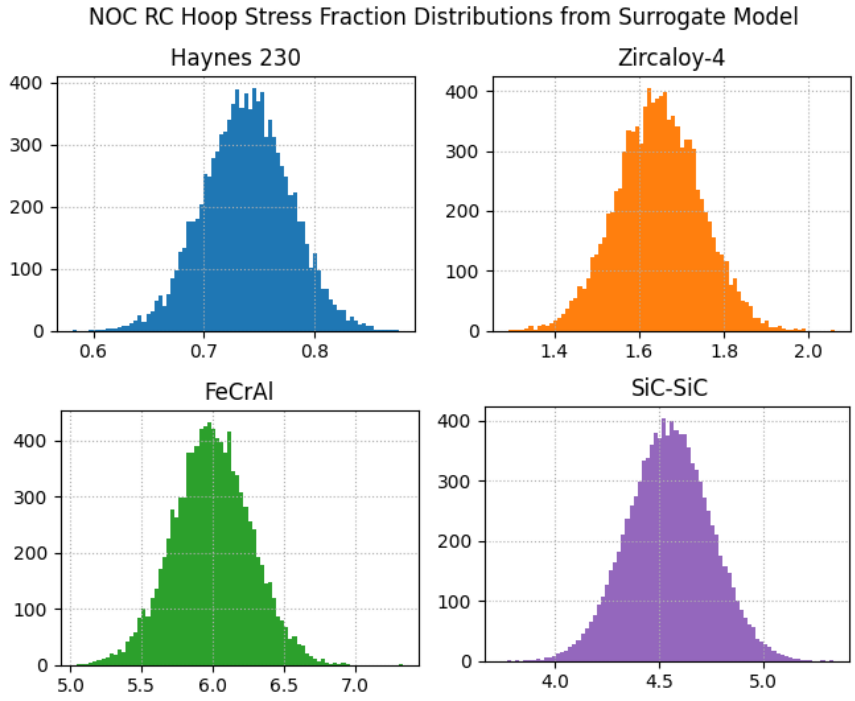

Figure 5.13. Distributions of ring clamp hoop stress fractions among the NOC surrogate model runs by candidate cladding.

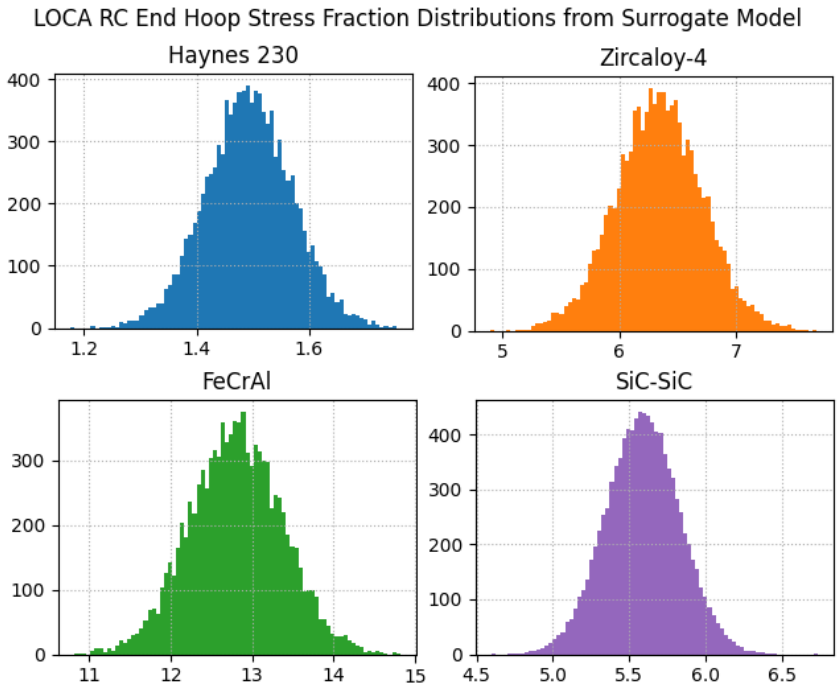

Figure 5.14. Distributions of ring clamp end timestep hoop stress fractions among the LOCA surrogate model runs by candidate cladding.

Table 5.1. Expected RC Hoop Stress Fractions by Model

	MOOSE	Surrogate	Surrogate Std Dev	Std Dev (% of Surrogate)
NOC Haynes 230	0.73816	0.73892	0.03879	4.5369
NOC Zircaloy-4	1.6390	1.6458	0.09858	5.2499
NOC SiC-SiC	4.5494	4.5491	0.19852	4.3639
NOC FeCrAl	5.9798	5.9928	0.27189	5.9897
LOCA End Haynes 230	1.4900	1.4924	0.07668	4.4774
LOCA End Zircaloy-4	6.3172	6.3384	0.37044	5.1382
LOCA End SiC-SiC	5.5884	5.5879	0.24233	4.3368
LOCA End FeCrAl	12.793	12.803	0.57326	5.8443

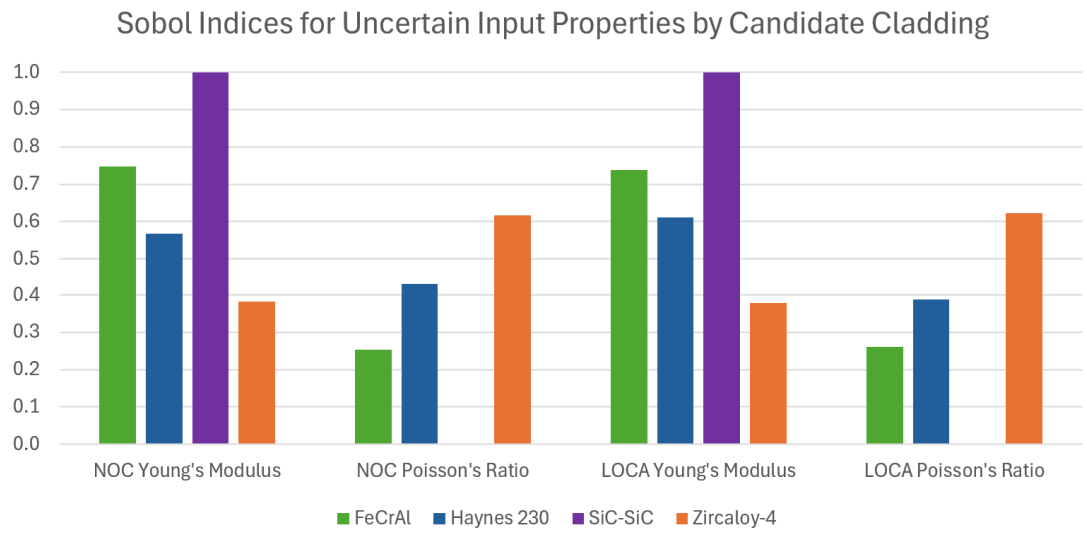

Figure 5.15. Sobol indices of the uncertain input parameters for both NOC and LOCA, colour-coded by candidate cladding.

6. CONCLUSIONS

This project was able to successfully replicate the neutronics, thermodynamics, heat transfer, and tensor mechanics of the NASA Kilopower reactor. Through it, this paper was able to compare the performances and failure limits of four candidate cladding materials in this reactor environment with parametric analyses.

There was little affect on the reactor's power profile from the candidates. Major differences came with the thermodynamic and heat transfer simulations, where Haynes 230 showed the most stress resistance and was the only material that stayed within its yield strength during normal operational conditions. Although none exhibited any danger of melting, SiC-SiC, as a ceramic, showed the most resistance to temperature change and in fact kept the core temperature lower as a result. Haynes 230's stress performance was the most noteworthy, meaning it can be deemed the best among the four for use in high-temperature microreactors.

This analysis has served to discourage investigations into Zircaloy-4, FeCrAl, and SiC-SiC's useage in Kilopower-like reactors. The high temperatures were the most likely limiting factor, as the first two candidates were designed for use in the low-temperature environments of light water reactors, where their material limits are generally much higher. SiC-SiC is afforded higher temperatures of operation, but its ceramic nature discourages elasticity, meaning it has a naturally low mechanical stress limit. Such discouragement is beneficial, as testing of nuclear materials is costly and time-intensive – resources which may be put toward investigations of other candidates.

Such material properties may be subject to variance, which may influence the previously found results. The project was also able to perform non-intrusive uncertainty quantification and sensitivity analysis on the simulation, creating a surrogate model to represent it. None of the candidates showed significant sensitivity to uncertainty in their

properties, although an investigation into Zircaloy-4's high temperature properties may be warranted, as its expected performance was close to stress failure, and further clarification of its properties may bring it within stress limits.

However, this methodology excluded other factors, such as material cost, ease of manufacture, or chemical interactions. Although it is easy to declare all but Haynes 230 as infeasible, reactor designs are subject to change as much as any other engineering project. Should a candidate have a substantial leg up on Haynes 230 in an area this paper did not cover, it may be prudent to change the subject reactor's design to accomodate this.

Future work is encouraged to look into the aforementioned factors comparing these four and potentially more candidate claddings. Kilopower is a rare example of a reactor that has been built and tested and offers a strong foundation for modeling and simulation. This paper was unable to obtain benchmarking unavailable to the public, so if more data is found, it would be wise to perform a review of this paper or even redo the work with this new information.

Additionally, this paper found a general lack of existing test data for these materials at high temperatures. A more robust library of their properties would greatly help modeling and simulation efforts, and could serve as a final answer for their advanced reactor application status.

NASA and many private interests are beginning their next thrust towards outer space, where Kilopower-like reactors will be needed in abundance and will be continuously iterated on. Therefore, further analysis on these topics will be of high demand and this project highly encourages it.

REFERENCES

[1] Neutron Bytes. NASA seeks industry proposals for compact nuclear power systems to be used in exploration of the moon and mars, 9 2020. Last accessed 31 December 2023.

[2] David I. Poston, Marc A. Gibson, Thomas Godfroy, and Patrick R. McClure. KRUSTY reactor design. *Nuclear Technology*, 206:S13–S30, 2020.

[3] Los Alamos National Lab. 'game changing' space-mission power system passes tests with flying colors, 5 2018. Last accessed 31 December 2023.

[4] Kevin G. Field, Mary A. Snead, Yukinori Yamamoto, and Kurt A. Terrani. Handbook on the material properties of fecral alloys for nuclear power production applications. *U.S. Department of Energy - Nuclear Technology R&D Advanced Fuels Campaign*, pages ORNL/TM–2017/186, 2017.

[5] Teng-Teng Xu, Su Cheng, Lai-Zhen Jin, Kun Zhang, and Tao Zeng. High-temperature flexural strength of SiC ceramics prepared by additive manufacturing. *International Journal of Applied Ceramic Technology*, 17(2):438–448, 2019.

[6] K. J. Geelhood, C. E. Beyer, and W. G. Luscher. PNNl stress/strain correlation for zircaloy. *Pacific Northwest National Lab*, pages PNNL–17700, 2008.

[7] Haynes International. Haynes 230 alloy, 2021. Last accessed 28 December 2023.

[8] Kurt A. Terrani. Accident tolerant fuel cladding development: Promise, status, and challenges. *Journal of Nuclear Materials*, 501:13–30, 2018.

[9] World Nuclear Association. Nuclear power reactor characteristics, 7 2015. Last accessed 28 December 2023.

[10] Office of Nuclear Energy. Advanced reactor technologies. Last accessed 27 December 2023.

[11] M. A Khattak, Abdoulhdi A. Borhana Omran, S. Kazi, M. S. Khan, Hafiz M. Ali, Syeda L. Tariq, and Muhammad A. Akram. A review of failure modes of nuclear fuel cladding. *Journal of Engineering Science and Technology*, 14:1520–1541, 2019.

[12] World Nuclear Association. Fukushima daiichi accident, 8 2023. Last accessed 28 December 2023.

[13] World Nuclear Association. Fukushima: Background on reactors. Last accessed 29 December 2023.

[14] United States Nuclear Regulatory Commission. Large light water reactors, 9 2022. Last accessed 28 December 2023.

[15] Marc Gibson, David Poston, Patrick McClure, Thomas Godfroy, Maxwell Briggs, and James Sanzi. The kilopower reactor using stirling technology (KRUSTY) nuclear ground test results and lessons learned. In *International Energy Conversion Engineering Conference 2018*, Cincinnati, Ohio, 2018.

[16] National Aeronautics and Space Association. NASA, DARPA will test nuclear engine for future mars missions. Last accessed 29 December 2023.

[17] National Aeronautics and Space Administration. NASA's lunar exploration program overview, 2020. Last accessed 27 December 2023.

[18] C. L. Whitmarsh. Review of zircaloy-2 and zircaloy-4 properties relevent to N.S. Savannah reactor design. *Oak Ridge National Lab*, pages ORNL–3281, 1962.

[19] Studying silicon carbide for nuclear fuel cladding. *Nuclear Engineering International*, 4 2013.

[20] Kazuma Kobayashi, Dinesh Kumar, Matthew Bonney, Souvik Chakrabortya, Kyle Paaren, Shoaib Usman, and Syed Alam. Uncertainty quantification and sensitivity analysis for digital twin enabling technology. *Springer Nature*, Handbook of Smart Energy Systems:2265—2277, 2023.

[21] Allegheny Technologies. Reactor grade zirconium. Last accessed 2 January 2024.

[22] T. Koyanagi, Y. Katoh, G. Jacobsen, and C. Deck. Handbook of LWR SiC/SiC cladding properties - revision 1. *U.S. Department of Energy - Nuclear Technology Research and Development Advanced Fuels Campaign*, pages ORNL/TM–2018/912, 2018.

[23] Thermalloys AB. FeCrAl alloys, 2012. Last accessed 2 January 2024.

[24] John Thomas Creasy. Thermal properties of uranium-molybdenum alloys: Phase decomposition effects of heat treatments. *Texas A&M University*, 2011.

[25] Los Alamos National Lab. MCNP® code version 6.3.0 theory & user manual. Last accessed 4 January 2024.

[26] Missouri S&T. The foundry. Last accessed 28 December 2023.

[27] Idaho National Laboratory. High performance computing. Last accessed 28 December 2023.

[28] Michael Oberguggenberger, Julian King, and Bernhard Schmelzer. Classical and imprecise probability methods for sensitivity analysis in engineering: A case study. *International Journal of Approximate Reasoning*, 50:680—693, 2008.

[29] Dinesh Kumar, Farid Ahmed, Shoaib Usman, Ayodeji Alajo, and Syed Bahauddin Alam. Recent advances in uncertainty quantification methods for engineering problems. *Academic Press*, AI Assurance:453–472, 2023.

[30] E. E. Lewis and Jr. W. F. Miller. *Computational Methods of Neutron Transport*. American Nuclear Society, 1993.

[31] Luka Snoj and Matjaž Ravnik. Calculation of power density with MCNP in TRIGA reactor. In *International Conference - Nuclear Energy for New Europe 2006*, Portorož, Slovenia, 9 2006.

[32] Christophe Geuzaine and Jean-François Remacle. Gmsh - a three-dimensional finite element mesh generator with built-in pre- and post-processing facilities. Last accessed 1 January 2024.

[33] Idaho National Lab GitHub. Heat transfer module. Last accessed 11 February 2024.

[34] Idaho National Laboratory. BISON: A finite element-based nuclear fuel performance code. Last accessed 28 December 2023.

[35] Marc A. Gibson, David I. Poston, Patrick R. McClure, James L. Sanzi, Thomas J. Godfroy, Maxwell H. Briggs, Scott D. Wilson, Nicholas A. Schifer, Max F. Chaiken, and Nissim Lugasy. Heat transport and power conversion of the kilopower reactor test. *Nuclear Technology*, 206:31–42, 2020.

[36] Idaho National Lab GitHub. Tensor mechanics master action system. Last accessed 12 February 2024.

[37] Idaho National Lab GitHub. Compute finite strain in cartesian system. Last accessed 12 February 2024.

[38] Idaho National Lab GitHub. Compute finite strain elastic stress. Last accessed 12 February 2024.

[39] Idaho National Lab GitHub. Compute isotropic elasticity tensor. Last accessed 12 February 2024.

[40] William S Slaughter. *The Linearized Theory of Elasticity*. Springer Science & Business Media, 2012.

[41] Monte Engelkemier. How to perform a pipe stress analysis, 9 2017. Last accessed 1 January 2024.

[42] Engineers Edge. Pressure vessel, thin wall hoop and longitudinal stresses. Last accessed 1 January 2024.

[43] Engineers Edge. Stress concentration fundamentals. Last accessed 1 January 2024.

[44] Dongbin Xiu and George Em Karniadakis. The wiener-askey polynomial chaos for stochastic differential equations. *SIAM Journal on Scientific Computing*, 24:619–644, 2002.

[45] J.D. Jakeman, F. Franzelin, A. Narayan, Dirk Plffiger, and M.S. Eldred. Polynomial chaos expansions for dependent random variables. *Sandia National Labs*, pages SAND2019–5228R, 2019.

VITA

Alexander Niles Foutch was born in Grand Rapids, Michigan on August 27, 1999. He attended schools in the Novi public school district and graduated from Novi High School in June 2017. For the 2017-2018 school year, he attended the University of Michigan in Dearborn under the Undecided Engineering program. In August 2018 he transferred to the Missouri University of Science & Technology in May 2021 received the degree of Bachelor of Science in Nuclear Engineering. He entered the graduate program for Missouri University of Science & Technology in August 2021 and received a Master of Science Degree in Nuclear Engineering in May 2024.